

Constraints on hydraulic properties from free pressure oscillations recorded during pumping operations in boreholes

Victoria Alegría Jiménez Martínez  and Jörg Renner

Institute for Geology, Mineralogy, and Geophysics, Ruhr-Universität Bochum, D-44780 Bochum, Germany. E-mail: Victoria.JimenezMartinez@rub.de

Accepted 2022 August 10. Received 2022 August 10; in original form 2022 March 28

SUMMARY

Free pressure oscillations during pumping operations in boreholes may potentially constrain hydraulic characteristics of the surrounding material. These damped oscillations occur when flow rate is suddenly changed, and their period and decay rate depend on the hydraulic properties of the entire hydraulic system: the porous medium, a section of the borehole, and/or the injection line, depending on test set-up. There have been previous attempts to estimate transmissivity values from free pressure oscillations that occurred during slug tests in open boreholes. The analysis used did not account for viscous losses due to the fluid interacting with the borehole wall. In contrast, dispersion relations of flow waves in a tight borehole (i.e. a cylindrical hole in an impermeable medium) account for wall friction. We extend a previous analytical treatment of flow waves by changing the boundary condition of the fluid velocity at the borehole wall to include fluid exchange between borehole and porous medium. In addition, we performed numerical modelling of waves propagating in boreholes with impermeable and permeable walls to assess the effect of the assumptions behind the analytical solution. We established how to distinguish cases in which the flow into the porous medium affects the oscillation characteristics (suitable for a hydraulic analysis) from those in which the equipment properties dominate the observations. Applying our methods to a range of field observations yielded plausible hydraulic property values of the rock volume surrounding the borehole.

Key words: Fracture and flow; Permeability and porosity; Fourier analysis; Numerical modelling.

1 INTRODUCTION

Several approaches employing observations of oscillatory pore-fluid pressure or flow-rate in boreholes have been followed to obtain hydraulic properties of permeable media (e.g. Bredehoeft 1967; Hsieh *et al.* 1987; Rasmussen *et al.* 2003; Renner & Messar 2006; Audouin & Bodin 2007; Gultinan & Becker 2015; Cheng & Renner 2018). Forced oscillations constitute externally controlled excitations of the hydraulic system causing responses that are easily distinguished from background perturbations using time-to-frequency transformations (e.g. Renner & Messar 2006). Forced oscillations, with a range of frequencies, might be induced by pumping operations (Rasmussen *et al.* 2003; Cheng & Renner 2018) or natural processes, for example tides (e.g. Bredehoeft 1967; Hsieh *et al.* 1987), barometric loading (e.g. Lai *et al.* 2013) and seasonal variations in precipitation (e.g. Saar & Manga 2003). Free oscillations, excited when an oscillator is displaced and quickly released (e.g. Halliday *et al.* 2011), known for a long time in tubes (Frizell 1898), reveal the natural frequency of the system. Free pressure oscillations were observed in boreholes after passing seismic waves (e.g. Bredehoeft *et al.* 1966) or after a rapid change in pumping parameters during hydraulic well testing, for example a slug test (e.g. Audouin & Bodin 2007; Krauss 1974; van der Kamp 1976; Kipp 1985).

Free pressure oscillations have mostly been considered a side effect when occurring during pumping operations in boreholes. The few previous models for these oscillations, aiming at the determination of hydraulic properties, interpreted the well-aquifer system as a classical mass-spring oscillator, relating the coefficients of a second-order damped oscillation equation to the aquifer parameters. The fluid in the borehole corresponds to the mass and the borehole storage capacity, providing a linear restoring force, to the spring. The storage capacity differs for open (Krauss 1974; van der Kamp 1976; Mcelwee & Zenner 1998) and closed (Weidler 1996) boreholes. In open boreholes, variations in water level and pressure are coupled and thus gravity acts as restoring force, while in closed wells, pressure variations cause compression of the borehole fluid and elastic well deformation. In general, these mass-spring models do not account for damping due to the interaction of the viscous fluid and the borehole wall, here addressed as wall friction, but solely consider damping due to fluid exchange between borehole and porous medium. We address the latter mechanism as ‘leakage’ irrespective of the direction of flow, which may actually

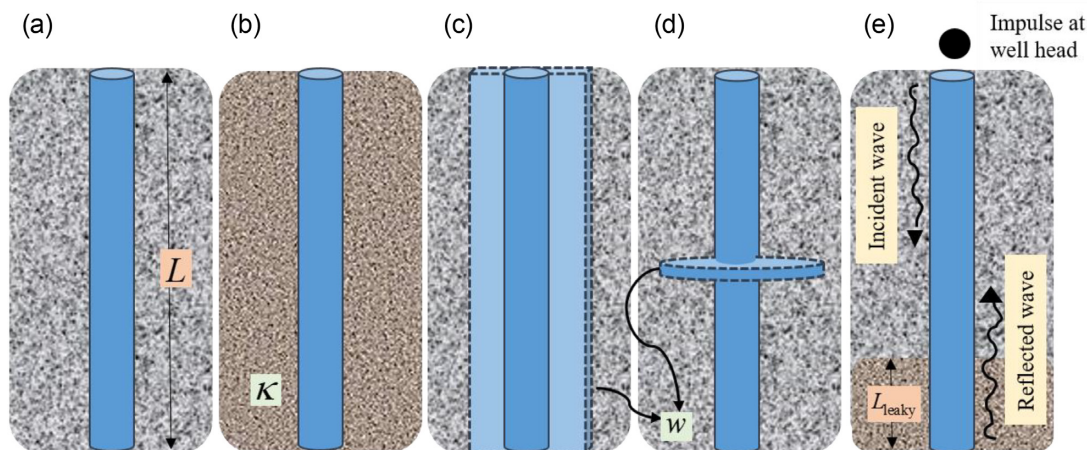


Figure 1. Sketch representing different scenarios considered where flow waves can propagate, that is a borehole of length L (a) in a tight porous medium, (b) in a homogeneous porous medium with permeability κ , in a tight porous medium intersected by a (c) vertical (axial) or (d) horizontal (radial) fracture with aperture w and (e) in a tight porous medium with a permeable interval of length L_{leaky} at the bottom.

reverse during an oscillation. One of the models that included losses due to wall friction was presented by Mcelwee & Zenner (1998), who considered the viscous losses a nonlinear mechanism in the second-order damped oscillator. However, the leakage aspect of the solution does not account for the storage coefficient of the porous medium since the fluid is treated as incompressible. Fischer (2016) used the model derived by Weidler (1996) to determine transmissivity values from oscillations observed during pumping operations in the boreholes Horstberg and Groß Buchholz, Germany. The derived transmissivity values exhibit a plausible order of magnitude but a counterintuitive decreasing trend over the course of the performed hydraulic stimulations.

The mass-spring models neglect the local coupling of the fluid compression and the deformation of the borehole due to the pressure variations. Viscous interaction between flowing fluids and the conduit walls was investigated for holes in rigid and deformable media (Bernabé 2009; Korneev 2010). Extensions of the basic concepts of solid–liquid interface waves, the so-called Stoneley waves (Chadwick & Borejko 1994), to tubes (boreholes) or slits (fractures) in impermeable or permeable solids (Tang & Cheng 1989; Tang 1990; Tang *et al.* 1991a) address the coupling between solid deformation and fluid pressure variations, yet neglect viscous interaction.

We aim to analyse free pressure oscillations recorded during pumping operations in boreholes to constrain hydraulic properties. The analysis of these oscillations requires the development of a theoretical framework that includes both loss mechanisms, leakage and wall friction. Therefore, we extended the analytical end-member model (Bernabé 2009) that accounts only for ‘wall friction’ by adding the effect of leakage. We complement the analytical models by numerical modelling of flow waves in impermeable and permeable boreholes solving the Navier–Stokes equations for compressible fluids. The goal of the numerical simulations is to quantify the effect of the two loss mechanisms on frequency and damping coefficient of a free pressure oscillation, accounting for conditions not considered in the analytical solutions, for example the finite length of the borehole, advective terms in the Navier–Stokes equations, and boreholes with permeable sections, only. Using the established analytical solutions and considering the numerical results, we analyse the suitability of a range of field observations, gained with vastly different set-ups, for an inversion of hydraulic parameters.

2 DISPERSION RELATIONS FOR WAVES IN BOREHOLES AND FRACTURES

We address mechanical waves in fluid-filled conduits, for example boreholes with radius R or fractures with aperture w , oscillating with frequency f as fluid-flow waves. The approximate conventional analysis familiar for organ pipes suggests that the finite length of a cylindrical hole, L , determines the frequency of standing fluid-flow waves as $f_0 = c_0/(4L)$ and $\hat{f}_0 = c_0/(2L)$ when both ends are and just one end is closed, respectively, where $c_0 = \sqrt{K_f/\rho_f}$ denotes the acoustic velocity of the fluid with bulk modulus K_f and density ρ_f . A borehole in an impermeable porous medium (Fig. 1a) may correspond to either endmember model, i.e. open or closed, depending on the conditions at the wellhead. A permeable section (Fig. 1b) or an intersecting fracture (Figs 1c–e) may affect the oscillation frequency, as these hydraulic elements compose ‘openings’ comparable to the holes in flutes (Forster 2010), but will inevitably lead to an increase in the damping coefficient as a consequence of loss of fluid from the borehole. This ‘leakage’, by which fluid-flow waves excited in the borehole diffuse into fractures or permeable media, is just one example for the coupling of fluid-flow waves with processes in the solid penetrated by the borehole. The flow in axial direction of the borehole gives rise to viscous interaction at the solid wall, and the pressure variations in the fluid cause deformation of the solid. Damping of free pressure oscillations may arise from any combination of leakage, wall friction, and solid deformation.

The dispersion relation, that is the frequency dependence of the wavenumber $k(\omega)$, where $\omega = 2\pi f$ denotes the angular frequency, expresses the physics of the wave propagation. Several simplifications regarding the coupling between the deformation of the fluid and the solid have been considered for the derivation of analytical dispersion relations of flow waves. For example, specific aspects of the coupling

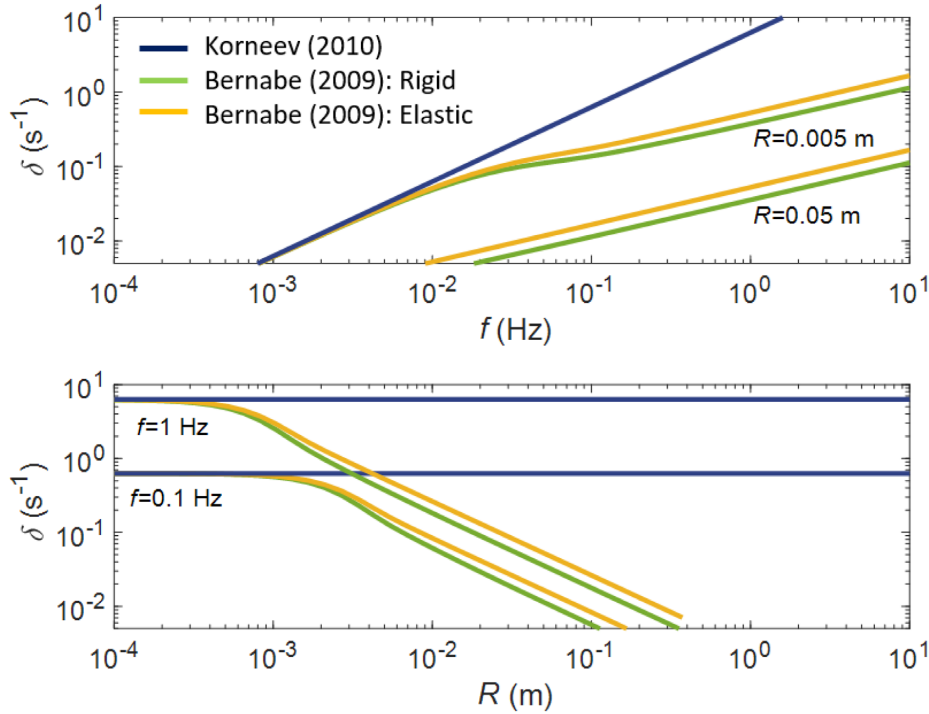


Figure 2. Damping coefficient as a function of (top) frequency and (bottom) pipe's radius calculated from the dispersion relations for flow waves in rigid (1) and elastic tight boreholes from Bernabé (2009) and Korneev (2010). The shear velocity used is 300 m s^{-1} to exaggerate the effect.

are excluded when the solid is assumed perfectly rigid. Solutions for coupled deformation of fluid and solid including viscous interaction at the borehole wall exist (e.g. Bernabé 2009) but do not include leakage at the conduit walls.

2.1 Fluid-flow waves in tight boreholes

We address boreholes that do not exchange fluid with the penetrated medium –over the timescale relevant for the free-pressure oscillations– as tight. Bernabé (2009) and Korneev (2010) analysed fluid-flow waves in such tight boreholes and specifically presented solutions of the continuity equation and the conservation of linear momentum (commonly addressed as the Navier–Stokes equation) for an infinite rigid pipe with a no-slip boundary condition for the fluid at the pipe wall. Specifically, Bernabé (2009) yield a dispersion relation relying on the long-wavelength approximation, i.e. $\lambda \ll L$ where λ is the wavelength of the fluid-flow wave, and neglecting advective terms:

$$k_z^2 = \frac{\omega^2}{c_0^2 \left[1 - \frac{2\nu J_1(\sqrt{2i}R/\nu)}{R J_0(\sqrt{2i}R/\nu)} \right]}, \quad (1)$$

where $\nu = \sqrt{2\mu_f/(\rho_f\omega)}$, known as viscous skin depth (e.g. Kurzeja *et al.* 2016) with μ_f the dynamic fluid viscosity, indicates the width of the boundary layer controlled by viscous forces, and $J_0(\cdot)$ and $J_1(\cdot)$ denote the Bessel functions of first kind of zero and first order, respectively. In deriving (1), Bernabé (2009) followed a ‘hybrid’ approach of accounting for the compressibility $\beta_f = 1/K_f$ of the fluid in the continuity equation but not in the Navier–Stokes equation and requested the pressure profile perpendicular to the flow to be flat, that is independent of the radial position in the fluid, as a consequence of the long-wavelength approximation.

According to (1), the propagation velocity of the fluid-flow wave in a rigid tube, $c(\omega) = \omega/k_z(\omega)$, increases with increasing frequency, asymptotically reaching the acoustic velocity of the fluid, and decreases with the decrease of the tubes radius. The damping coefficient of these waves, conveniently integrated by the use of complex wavenumbers (Georgi 2015), see also Appendix A, is the larger the more the viscous forces dominate, that is $\nu \gg R$. The dispersion relation of the Biot-regime presented by Korneev (2010) is equal to (1) in the limit of low-frequency and/or small borehole radius (Fig. 2).

In the course of the derivation of the solution for a borehole in an elastic medium, Bernabé (2009) made a number of approximations regarding the relative size of terms involving Bessel functions, owing to which the dispersion relation depends only on the ability of the solid to shear, represented by its shear wave velocity V_s , but not on the bulk modulus of the solid. The dispersion relation is a fourth-order polynomial (see eq. 46 in Bernabé 2009), which has two physical solutions, a fast and a slow wave (Kurzeja *et al.* 2016). Damping of the slow wave converges to the damping of a fluid-flow wave in a borehole with rigid walls (1) when $V_s > c_0$ but exceeds that value when $V_s < c_0$. This increase in damping coefficient can be up to twice the value of a borehole with rigid walls for a porous medium with a shear velocity as low as $V_s = 300 \text{ m s}^{-1}$ (Fig. 2).

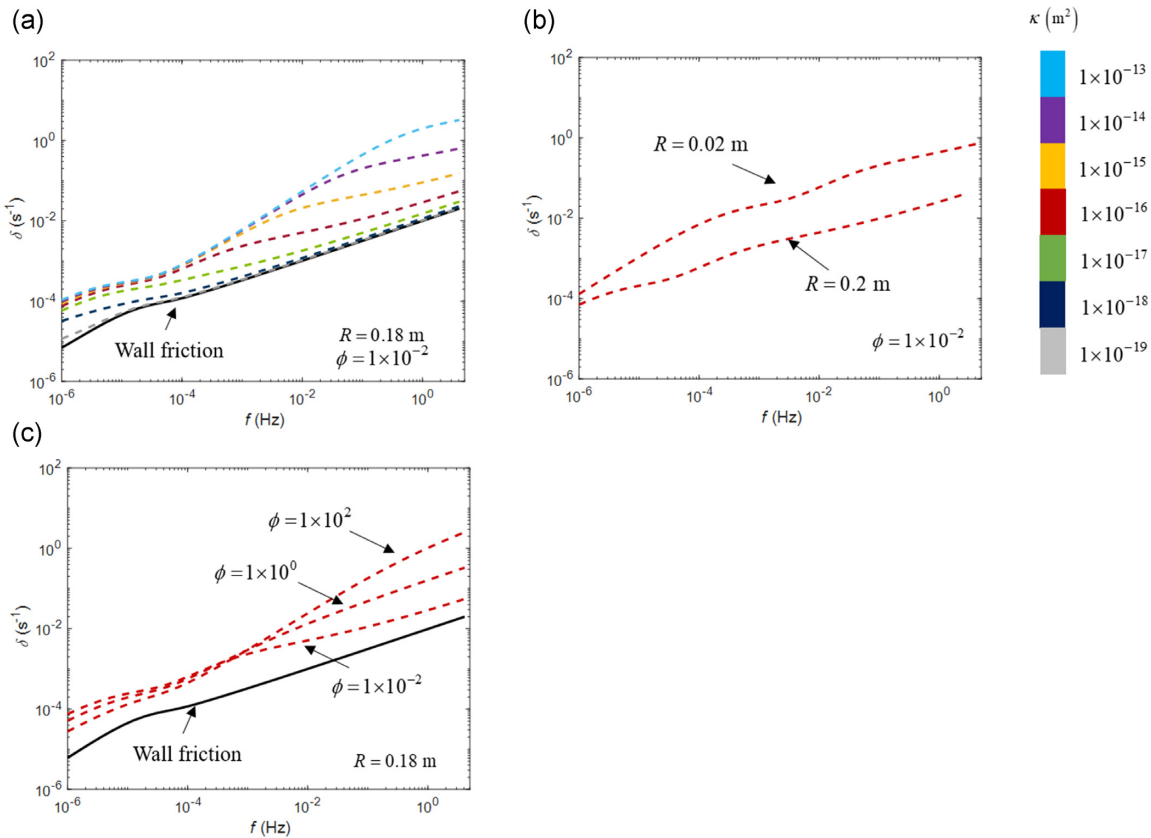


Figure 3. Relation between damping coefficient and frequency of a free oscillation propagating in a leaky borehole for different (a) permeabilities, (b) porosities and (c) borehole radius according to (2).

2.2 Fluid-flow waves in leaky boreholes

We address boreholes in a rock whose hydraulic properties allow for fluid exchange with the borehole—on the characteristic timescale of the fluid-flow wave—as leaky. A fluid-flow wave travelling in a leaky borehole is attenuated due to the irreversible flow between the borehole and the permeable rock. We obtained a dispersion relation for a fluid wave traveling in a leaky borehole that extends Bernabé’s (2009) approximate analytical solution (1) by modifying the boundary condition at the borehole wall to account for radial flow in a purely diffusive process between the borehole and the porous medium (Appendix B):

$$\frac{J_1(\sqrt{2i}R/v)}{J_0(\sqrt{2i}R/v)} \frac{\sqrt{2i}\mu_f}{v\rho_f^2\omega^2} k_z^2 + \frac{1}{v^2} i\mu_f R \left(\frac{\omega^2 - c_0^2 k_z^2}{\rho_f^2 \omega^2 c_0^2} \right) = -\frac{\kappa_{\text{eff}}}{\mu_f} \sqrt{k_z^2 - \frac{i\omega}{D}} \frac{K_1\left(R\sqrt{k_z^2 - \frac{i\omega}{D}}\right)}{K_0\left(R\sqrt{k_z^2 - \frac{i\omega}{D}}\right)}. \tag{2}$$

We relate the effective permeability in (2) to material properties, and fracture and borehole geometry depending on the type of considered conduit (Appendix B) by

$$\kappa_{\text{eff}} = \begin{cases} \kappa & \text{for a homogenous porous medium} \\ \frac{L_{\text{leaky}}}{L} \kappa & \text{for an open-hole section} \\ \frac{w^3 L_F}{12\pi RL} & \text{for a pair of axial fractures} \\ \frac{w^3}{12L} & \text{for a radial fracture} \end{cases}. \tag{3}$$

The dispersion relation (2) depends on permeability, diffusivity, and borehole radius, all affecting the damping coefficient of the flow wave traveling in the leaky borehole. For an impermeable rock ($\kappa_{\text{eff}} \rightarrow 0$), the dispersion relation (2) reduces to (1), which constitutes the lower bound for the frequency-dependent damping coefficients (Fig. 3a). The effect of borehole radius on wall friction is as for tight boreholes, that is the damping coefficient increases with decreasing borehole radius (Fig. 3b). Damping increases with effective permeability at given frequency (Fig. 3a). A decrease in diffusivity leads to an increase in damping coefficient (Fig. 3c). For a given effective permeability, diffusivity decreases when the storage capacity, in the following represented by apparent porosity $\phi_{\text{app}} = s_{\text{eff}} K_f$, increases. Apparent porosity represents the porosity of a hypothetical porous medium with a rigid skeleton exhibiting the specific storage capacity of the real medium; apparent porosity thus exceeds the true porosity since it attributes any contribution of skeleton deformation to specific storage capacity to a

Table 1. Properties of the fluid (water) used in the simulations.

ρ_f (kg m ⁻³)	μ_f (Pa s)	β_f (Pa ⁻¹)
1000	0.001	4.16E-10

Table 2. Spectral components of free pressure oscillation obtained by varying fluid compressibility in a tight borehole of 1 m length and 0.004 m radius. Fluid velocity, nominal fundamental frequency and viscous skin depth depend on fluid compressibility.

β_f (Pa ⁻¹)	c_0 (m/s)	f_0 (Hz)	v (m)	R/v (-)	f (Hz)	Δf (Hz)	δ (s ⁻¹)	$\Delta\delta$ (s ⁻¹)
4.16E-09	4.90E+02	1.22E+02	5.10E-05	7.85E+01	1.2E+02	1.2E-01	5.4E+00	3.0E-01
4.16E-10	1.55E+03	3.87E+02	2.87E-05	1.40E+02	3.8E+02	2.0E-01	2.4E+01	1.4E+01
4.16E-11	4.90E+03	1.22E+03	1.61E-05	2.48E+02	1.2E+03	2.2E-01	1.0E+02	1.4E+01

compressible pore fluid (e.g. Schepp & Renner 2021). Thus, fractured media may reach apparent porosity values even exceeding 100 per cent by large owing to the exceptional deformability of fractures (e.g. Fischer & Paterson 1992).

The effect of deformability of the solid medium housing a tight borehole on damping is limited (Fig. 2) as demonstrated by Bernabé (2009). In contrast, specific storage capacity, partly related to the effective deformability of the solid, significantly affects the dispersion relation (e.g. Fig. 3c). While physically inconsistent, it is therefore legitimate to use the rigid borehole formulation (1) and still allow for specific storage capacity values corresponding to deformable media.

3 NUMERICAL MODELLING

Our numerical modelling focuses on the attenuation of fluid-flow waves in boreholes filled with water (Table 1) in impermeable and permeable, rigid, solid media to resemble the conditions of the analytical solutions (1) and (2), respectively. In contrast to the analytical approach, the numerical simulations treat boreholes of finite length allowing for standing waves. We also simulated flow waves in boreholes with a leaky section of length $L_{\text{leaky}} < L$ at their bottom, a scenario not covered by the analytical solutions. The resulting pressure oscillations were analysed as described in Appendix C.

Performing the numerical simulations also had the intention to assess whether any of the approximations inherent in the analytical solutions are problematic regarding their use for typical borehole scenarios. Unfortunately, the numerical simulations exhibited their own problems, a mesh-dependence of the results as detailed in Appendix D. Specifically, we found that the damping coefficient gained from numerical simulations exceeds that predicted by the analytical solution (1) when the size of the mesh element closest to the borehole wall is larger than the viscous skin depth.

3.1 Significance of approximations

The mesh-dependence of the numerical results complicates the assessment of the significance of approximations made for the analytical solutions (1) and (2). Yet, from an *a posteriori* evaluation, we can say with confidence, however, that the long-wavelength approximation underlying the analytical solutions holds for all considered model geometries in our simulations.

It is generally difficult to analytically assess the implications of the hybrid treatment of fluid compressibility in the analytical solution, that is accounted for in the continuity equation but neglected in the Navier–Stokes equation (Kreiss *et al.* 1991; Fischer 2015). We therefore varied the fluid compressibility over two orders of magnitude in numerical simulations (Table 2). The numerical results coincide with the analytical solution for a fluid with 10 times the compressibility of water but for lower compressibility the numerical damping coefficients exceed the analytical ones (Fig. 4). The agreement of the numerical results with the analytical predictions for highly compressible fluids suggests that the hybrid treatment of fluid compressibility in the analytical treatment is legitimate. The discrepancies found for fluids as incompressible as water result from the associated decrease in viscous skin depth (a low compressibility leads to an increase in oscillation frequency) giving rise to the problems identified from the presented mesh-dependence analysis (Appendix D).

The neglect of advective inertia terms in the approximate analytical treatment of the Navier–Stokes equations may lead to an underestimation of damping. Without a detailed explanation, Bernabé (2009) states that the neglect is not identical but in accord with the long-wavelength approximation. The classical dimensional analysis reveals that the neglect is valid for sufficiently large Strouhal numbers (Appendix E). The Strouhal numbers of our numerical models, calculated analytically and *a posteriori* using frequency and amplitude of the simulated free pressure oscillation, are of the order of $St_{\text{axial}} \sim 10^9$ and $St_{\text{radial}} \sim 10^{11}$ for the axial and radial velocity component, respectively (Appendix E) supporting the neglect of advective terms in the analytical solution (1).

3.2 Results

The vast majority of simulations yield underdamped pressure oscillations that are in cases visibly multimodal in the time domain (Fig. 5). Owing to the step-like excitation, the pressure responses exhibit harmonics of the fundamental frequency (higher modes), as evidenced

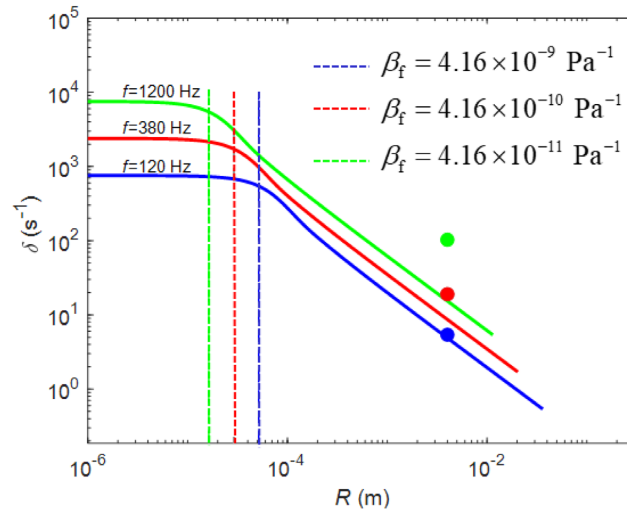


Figure 4. Effect of fluid bulk modulus on analytical (solid lines), that is according to (1), and on numerical (filled dots) damping coefficients for free pressure oscillations in a borehole of 1 m length and 0.004 m radius. Vertical dashed lines indicate the viscous skin depth .

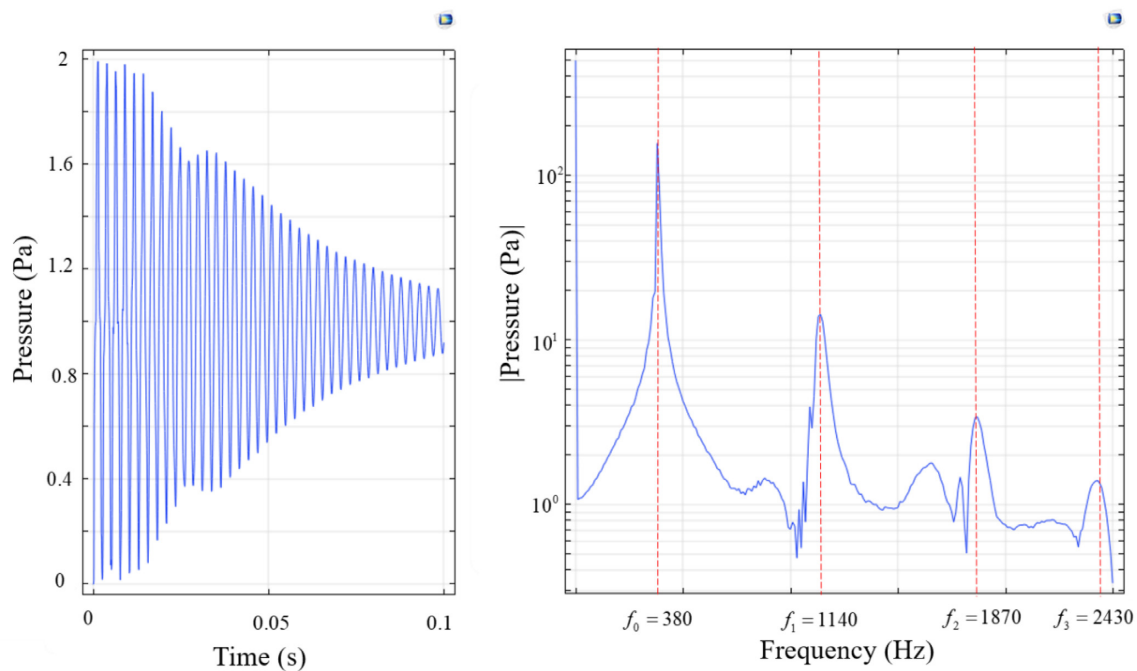


Figure 5. Free pressure oscillation in (left) time and (right) frequency domain resulting for the simulation performed in COMSOL in a borehole of 1 m length with a radius of 0.004 m. The red dashed lines signify the local maxima in the frequency spectrum that correspond to the fundamental frequency and its odd multiples (harmonics) indicated in red calculated using the conventional organ–pipe relations.

by the frequency spectrum (Fig. 5). Frequencies of the free pressure oscillations obtained in numerical simulations for tight (Table 3) and leaky boreholes (Table 4) are consistent with the theoretical prediction of the nominal eigenfrequency of the classic organ–pipe relation for a borehole with one open end for small damping coefficients. With increasing damping, frequencies of the numerical oscillations decreased from the nominal eigenfrequency reaching as little as 40 per cent reduction (Table 4). Frequencies of the numerical oscillations are lower than the ones expected for a damped harmonic oscillator, that is $f_\delta = \sqrt{(2\pi f_0)^2 - \delta^2/2\pi}$, by up to a factor of 1.5, but this discrepancy might result from the overestimation of the damping coefficients due to the identified meshing-problems (Appendix D), and we thus cannot evaluate whether the boreholes can be approximated as harmonic oscillators.

Damping coefficients increased when the viscous layer approached the radius of the borehole, for tight and leaky boreholes. In full- and partial-length leaky boreholes, damping coefficients increased with the increase of permeability and/or length of the leaky section, respectively. Damping coefficients exhibit significant differences between numerical results and analytical predictions (see Appendix D). The discrepancies are not caused by the differences in the level of approximation of the analytical solution but reflect that the used mesh

Table 3. Spectral components of the fundamental mode of pressure oscillations gained from the numerical modelling of tight boreholes.

L (m)	R (m)	ν (m)	R/ν (-)	f (Hz)	$P2_\nu + P2_p$	MFT	$P1_\nu + P1_p$	δ (s ⁻¹)
					Prony		Prony	
1	0.01	2.9E-05	3.5E+02	3.8E+02	1.5E+01 ± 1.5E+00	3.8E+02	3.8E+02	1.1E+01
1	0.004	2.9E-05	1.4E+02	3.8E+02	2.0E+01 ± 5.7E-01	3.8E+02	3.8E+02	1.4E+01
1	0.001	2.9E-05	3.5E+01	3.8E+02	3.6E+01 ± 2.0E-02	3.8E+02	3.8E+02	5.1E+01
4	0.04	5.8E-05	6.9E+02	9.6E+01	4.1E+00 ± 4.5E-01	9.6E+01	-	-
4	0.01	5.8E-05	1.7E+02	9.5E+01	5.7E+00 ± 6.5E-01	9.5E+01	-	-
4	0.004	5.8E-05	6.9E+01	9.5E+01	7.1E+00 ± 7.3E-01	9.5E+01	-	-
4	0.001	5.9E-05	1.7E+01	9.2E+01	1.9E+01 ± 1.0E+00	9.2E+01	-	-
4	0.0004	6.0E-05	6.7E+00	8.8E+01	5.5E+01 ± 1.5E+00	9.0E+01	-	-
8	0.04	8.1E-05	4.9E+02	4.8E+01	1.2E+00 ± 8.0E-02	4.9E+01	4.7E+01	1.6E+00
8	0.001	8.3E-05	1.2E+01	4.6E+01	1.2E+01 ± 5.8E-01	4.8E+01	4.5E+01	1.7E+01
100	0.1	2.9E-04	3.4E+02	3.7E+00	1.4E-01 ± 5.7E-03	3.8E+00	3.8E+00	3.0E-01
100	0.01	2.9E-04	3.4E+01	3.7E+00	5.3E-01 ± 2.1E-02	3.7E+00	3.5E+00	1.2E+00
100	0.004	2.9E-04	1.4E+01	3.7E+00	8.5E-01 ± 2.5E-02	3.7E+00	3.6E+00	1.4E+00
1000	0.1	9.3E-04	1.1E+02	3.7E-01	3.5E-02 ± 2.5E-03	3.7E-01	3.5E-01	1.1E-01
1000	0.04	9.3E-04	4.3E+01	3.7E-01	5.3E-02 ± 4.5E-03	3.7E-01	3.5E-01	1.2E-01

Table 4. Spectral components of the fundamental mode of pressure oscillations gained from the numerical modelling of leaky boreholes. All simulations were performed assuming an isotropic porous medium using the fluid polynomial interpolating function $P2_\nu + P2_p$ except for the cases marked with *.

κ (m ²)	L (m)	L_{leaky}/L (-)	R (m)	ν (m)	R/ν (-)	f (Hz)	Prony	MFT
							δ (s ⁻¹)	f (Hz)
1E-18	1000*	1	0.18	9.15E-04	1.97E+02	3.80E-01	3.23E-02 ± 2.36E-03	3.80E-01
1E-17	1000*	1	0.18	9.15E-04	1.97E+02	3.80E-01	3.48E-02 ± 3.20E-03	3.80E-01
1E-16	1000*	1	0.18	9.15E-04	1.97E+02	3.80E-01	1.05E-01 ± 5.77E-03	3.80E-01
1E-15	1000*	1	0.18	9.75E-04	1.85E+02	3.35E-01	7.08E-01 ± 4.10E-01	3.80E-01
1E-14	1000*	0.001	0.18	9.29E-04	1.94E+02	3.69E-01	3.23E-02 ± 9.57E-04	3.80E-01
1E-15	1000*	0.001	0.18	9.28E-04	1.94E+02	3.70E-01	4.48E-02 ± 9.57E-04	3.70E-01
1E-16	1000*	0.01	0.18	9.28E-04	1.94E+02	3.70E-01	4.68E-02 ± 9.57E-04	3.70E-01
1E-15	1000*	0.01	0.18	9.28E-04	1.94E+02	3.70E-01	5.38E-02 ± 9.57E-04	3.70E-01
1E-18	100	1	0.01	2.93E-04	3.41E+01	3.70E+00	5.80E-01 ± 2.00E-02	3.79E+00
1E-17	100	0.02	0.01	2.89E-04	3.46E+01	3.80E+00	4.30E-01 ± 5.00E-03	3.76E+00
1E-17	100	0.1	0.01	2.93E-04	3.41E+01	3.70E+00	8.00E-01 ± 2.60E-02	3.79E+00
1E-17	100	0.2	0.01	2.93E-04	3.41E+01	3.70E+00	1.23E+00 ± 5.70E-02	3.79E+00
1E-17	100	0.5	0.01	2.93E-04	3.41E+01	3.70E+00	2.23E+00 ± 5.70E-02	3.78E+00
1E-17	100	0.8	0.01	2.93E-04	3.41E+01	3.70E+00	2.60E+00 ± 5.70E-02	3.77E+00
1E-17	100	1	0.01	2.93E-04	3.41E+01	3.70E+00	2.60E+00 ± 5.70E-02	3.74E+00
1E-16	100	0.02	0.01	2.89E-04	3.46E+01	3.80E+00	7.80E-01 ± 7.20E-02	3.75E+00
1E-16	100	0.1	0.01	2.93E-04	3.41E+01	3.70E+00	5.10E+00 ± 5.70E-03	3.80E+00
1E-16	100	0.2	0.01	3.06E-04	3.27E+01	3.40E+00	9.90E+00 ± 4.30E-04	3.80E+00
1E-15	100	0.001	0.01	2.89E-04	3.46E+01	3.80E+00	5.90E-01 ± 5.10E-02	3.76E+00
1E-15	100	0.01	0.01	2.97E-04	3.36E+01	3.60E+00	3.60E+00 ± 1.80E-02	3.60E+00
1E-15	100	0.02	0.01	2.97E-04	3.36E+01	3.60E+00	4.50E+00 ± 2.00E-01	3.76E+00
1E-14	100	0.001	0.01	2.93E-04	3.41E+01	3.70E+00	1.48E+00 ± 5.70E-02	3.60E+00
1E-14	100	0.01	0.01	3.72E-04	2.69E+01	2.30E+00	7.20E+00 ± 5.10E-03	2.70E+00
1E-13	100	0.001	0.01	3.15E-04	3.17E+01	3.20E+00	3.25E+00 ± 1.52E-01	3.30E+00
1E-17	400	0.01	0.01	5.88E-04	1.70E+01	9.20E-01	1.95E-01 ± 1.10E-02	9.20E-01
1E-17	400	0.1	0.01	5.87E-04	1.70E+01	9.23E-01	3.10E-01 ± 9.50E-03	9.20E-01
1E-17	400	0.8	0.01	5.87E-04	1.70E+01	9.23E-01	9.33E-01 ± 3.20E-02	9.20E-01
1E-17	400*	0.8	0.01	5.85E-04	1.71E+01	9.20E-01	9.30E-01 ± 2.94E-02	9.20E-01
1E-18	4	1	0.01	5.79E-05	1.73E+02	9.50E+01	6.00E+00 ± 3.60E-02	9.54E+01
1E-17	4	1	0.01	5.79E-05	1.73E+02	9.50E+01	7.80E+00 ± 4.10E-02	9.56E+01
1E-16	4	1	0.01	5.79E-05	1.73E+02	9.50E+01	4.20E+01 ± 1.20E-03	9.52E+01

size is insufficient to resolve the velocity gradient for small viscous skin depths. The numerical damping coefficients compare well with the analytical ones when the radius of the first element close to the borehole wall is close to the viscous skin depth.

Inversion of frequency and damping coefficient towards permeability gives values above the values prescribed in the numerical model as a result of the overestimation of the damping coefficient. Nevertheless, the inverted permeability increases with the increase of the leaky section of the borehole for partial-length leaky boreholes (see Appendix D).

Table 5. Set-up parameters of the considered field campaigns during which free pressure oscillations were recorded. The expected fundamental frequency of the free pressure oscillation is calculated according to the organ–pipe relation using the total length of the system for the two end-conditions.

Site, borehole	Pipe radius (m)	Interval radius (m)	Total length (m)	Interval length (m)	Fundamental frequency (Hz)		Nyquist frequency (Hz)	comment
					One open end	Closed ends		
<i>Double-packer intervals</i>								
Calibration experiment	0.005	0.038	41	0.7	9	18	10	Tubes with fittings
Freiberg, BH10	0.005	0.038	41 to 59	0.7	6.5–9	13–17	2.5 and 10	Tubes with fittings
Hong Kong	0.004	0.038	301	0.7	1.25	2.5	2.5	Coiled tubing
<i>Cased wells</i>								
KTB, HB	0.14	0.18	9100	70	0.04	0.08	2.5	
Horstberg	0.10	0.18	4000	2 and 4	0.09	0.19	0.5	
Groß Buchholz, GT1	0.18	0.18	4000	2	0.09	0.19	0.5	Deviated

3.3 Implications for the analysis of field data from the comparison of numerical and analytical results

Analytical relations have obvious benefits for an inversion of field observations compared to numerical simulations. However, the analytical solution (1) is based on approximations whose consequences are to some extent hard to predict, for example regarding the incomplete account of fluid compressibility. We assessed the significance of these approximations by numerical results that in turn exhibited limitations related to insufficient mesh density near the borehole wall (Appendix D). These numerical problems strongly affected the damping coefficients of the simulated free pressure oscillations.

The analytical dispersion relations for infinitely long boreholes do not predict which frequency will be observed for a borehole with finite length. As shown by our numerical results, the frequencies of flow waves in tight, leaky or partially leaky boreholes are well approximated by the conventional length–relation for the appropriate end-condition, i.e. the classic organ–pipe relation, using the entire borehole length even for partially leaky boreholes. Dissipation due to the two mechanisms of wall friction and leakage reduces the frequency, qualitatively similar to what is known for a damped harmonic oscillator. As long as the oscillation is far from being overdamped, that is $\delta < 2\pi f_0$, the observed frequencies are, however, indicative of the length and the end condition of the fluid column, in which fluid waves interfere to form standing waves.

The analytical dispersion relations (1) and (2) predict the damping coefficient of a free oscillation in a tight or leaky borehole with finite length for given radius, fluid viscosity, and effective permeability and storage capacity of the porous medium. For tight and full-length leaky boreholes, the numerical damping coefficients are equal to or exceeded the analytical ones. Our numerical tests for tight boreholes demonstrate that the overestimation of numerical damping coefficients relative to the analytical ones results from insufficient resolution of the velocity profile close to the borehole wall. The resolution problem is aggravated for leaky boreholes since the velocity gradient close to the borehole wall also controls pressure diffusion into the porous medium. Modelling fractures intersecting the borehole would require an even finer mesh inside the fracture than the mesh required for the borehole alone to solve the velocity gradient inside the fracture. A dedicated code would be needed that generates meshes sufficiently fine in radial direction to capture the strong velocity changes in radial direction within the viscous skin depth.

Based on our theoretical and numerical analyses, we propose a sequential workflow for the evaluation of free oscillations recorded during pumping operations in boreholes. First, their spectral components, i.e. frequency and damping coefficient, are determined using Prony analysis, assisted by FFT and/or MFT. In the second step, frequency is assessed in the light of the conventional organ–pipe relations accounting for possible reduction due to damping. Actually, the two end conditions considered for the classic organ–pipe relations, i.e. open or closed, are just endmembers of the frequency of a flow wave in a borehole; the frequency is a continuous function of the storage capacity of a reservoir, S_{res} , at the tube’s end(s) (Appendix F). The two endmembers ‘open’ and ‘closed’ correspond to $S_{\text{res}} \rightarrow \infty$ and $S_{\text{res}} \rightarrow 0$, respectively. In the final step, the spectral components are compared to the dispersion relation for a tight borehole (1) to assess whether the damping is due to wall friction or due to leakage. If the damping coefficient is similar to that given by (1), hydraulic analysis is not possible, since the oscillations are likely governed by wall friction. A damping coefficient significantly above the limit given by (1) promises a sensible hydraulic analysis based on (2). In the sequel, we apply the proposed workflow to free-oscillation observations from five field tests with different set ups to investigate whether significant hydraulic properties can be deduced from them.

4 FIELD EXPERIMENTS

The field data are from five different campaigns with a range of set-ups that include double-packer intervals and cased wells with open-hole or perforated sections (Table 5). These tests constitute examples of partial leakage close to the bottom of the borehole where the length of the leaky section is less than 2 per cent of the total length of the system. The open-hole sections occur in long boreholes, i.e. more than 4000 m length, with a similar diameters of the injection line and the open-hole section. The deviation of one of the boreholes may cause dissipation not addressed by our modelling.

Table 6. Spectral components of free pressure oscillations derived from numerical simulations for a borehole of 1 m length using different mesh sizes and two types of meshes (see Fig. D1).

Mesh	R (m)	Order	f (Hz)	δ (s ⁻¹)	r_e (m)	ν (m)
ext.coarse	0.004	1	380	24	2.5E-04	2.9E-05
ext.coarse	0.004	3	1129.2	120	2.5E-04	1.7E-05
ext.coarse	0.004	5	1862	200	2.5E-04	1.3E-05
ext.coarse	0.004	7	2608.5	260	2.5E-04	1.1E-05
coarse	0.004	1	383	14	1.0E-04	2.9E-05
coarse	0.004	3	1137	70	1.0E-04	1.7E-05
coarse	0.004	5	1881.6	130	1.0E-04	1.3E-05
coarse	0.004	7	2635	190	1.0E-04	1.1E-05
fine	0.004	1	383.6	13	6.2E-05	2.9E-05
fine	0.004	3	1142.3	48	6.2E-05	1.87E-05
fine	0.004	5	1898.6	88	6.2E-05	1.3E-05
fine	0.004	7	2651.6	150	6.2E-05	1.1E-05
purely triangular	0.004	1	381	17	1.8E-04	2.9E-05
purely triangular	0.004	3	1132.5	93	1.8E-04	1.7E-05
purely triangular	0.004	5	1866.9	170	1.8E-04	1.3E-05
purely triangular	0.004	7	2615.4	260	1.8E-04	1.1E-05
purely triangular	0.004	1	382.9	14	9.0E-05	2.9E-05
purely triangular	0.004	3	1138	52	9.0E-05	1.7E-05
purely triangular	0.004	5	1888	100	9.0E-05	1.3E-05
purely triangular	0.004	7	2629	180	9.0E-05	1.1E-05
ext.coarse	0.001	1	377.7	37	1.1E-04	2.9E-05
ext.coarse	0.001	3	1124	170	1.1E-04	1.7E-05
ext.coarse	0.001	5	1872	320	1.1E-04	1.3E-05
ext.coarse	0.001	7	2589	540	1.1E-04	1.1E-05
coarse	0.001	1	380.5	37	5.0E-05	2.9E-05
coarse	0.001	3	1136.4	82	5.0E-05	1.7E-05
coarse	0.001	5	1875.6	140	5.0E-05	1.3E-05
coarse	0.001	7	2617.1	200	5.0E-05	1.1E-05
fine	0.001	1	380.3	37	3.0E-05	2.9E-05
fine	0.001	3	1138.9	85	3.0E-05	1.7E-05
fine	0.001	5	1883.1	130	3.0E-05	1.3E-05
fine	0.001	7	2643.1	230	3.0E-05	1.1E-05

The double-packer set-ups are characterized by injection lines with 7 to 20 times smaller radius of tubes (and hoses) connecting the probe with the surface and the tested well interval. Since the considered intervals are also much shorter than the associated injection lines, they may constitute a ‘boundary condition’ for the flow wave, i.e. the pressure is ‘instantaneously’ uniform in it, rather than a ‘change in tube diameter’, see Appendix F. The fittings between the injection tubes (and hoses) may give rise to turbulence and thus enhanced effective wall friction.

In all field tests except one of the double-packer set-ups (see Reiche Zeche and Calibration test in Table 5), the Nyquist frequency exceeded the fundamental frequency calculated for boreholes with one open and two closed ends using the total length of the specific system (Table 5). Thus, aliasing cannot be ruled out if the Nyquist frequency is not higher than the fundamental frequency of a borehole with two closed ends. In all other cases, the observed oscillations should reflect the true frequency. We analysed the recorded free pressure oscillations using the procedure applied to the numerical results, that is FFT, MFT and Prony analysis. We would like to point out that the viscous skin depths corresponding to the frequencies of observed oscillations fall in the range, for which the deviations of the numerical results from the analytical model (2) are still modest (Fig. D8).

The analytical solution for fluid flow waves in infinitely long leaky boreholes (2) assumes that the radial fluid velocity is equal to Darcy’s law at any ‘depth’. For boreholes with finite length or leaky sections, the boundary condition for the fluid exchange between borehole and formation is accounted for by the volume balancing leading to effective permeabilities (3). In practical applications, the ‘true hydraulic’ length of a leaky section is often unknown motivating the use of hydraulic transmissivity that reflects the hydraulic characteristics of a borehole rather than a medium. The relation between borehole and medium properties reads $T = \rho_f g L_{\text{leaky}} \kappa / \mu_f$, where g is the gravitational acceleration.

4.1 Cased wells with perforations or open-hole sections

4.1.1 Field equipment and site description

4.1.1.1 Horstberg and Groß Buchholz The boreholes Groß Buchholz GT1 and Horstberg are located at the outskirts and about 80 km NE of Hannover, respectively. The two cased boreholes have lengths of about 4000 m. Borehole Horstberg is vertical while Groß Buchholz is deviated 30° on its final 800 m. A range of pumping operations aimed to stimulate perforated Bunter sandstone sections close to the bottom

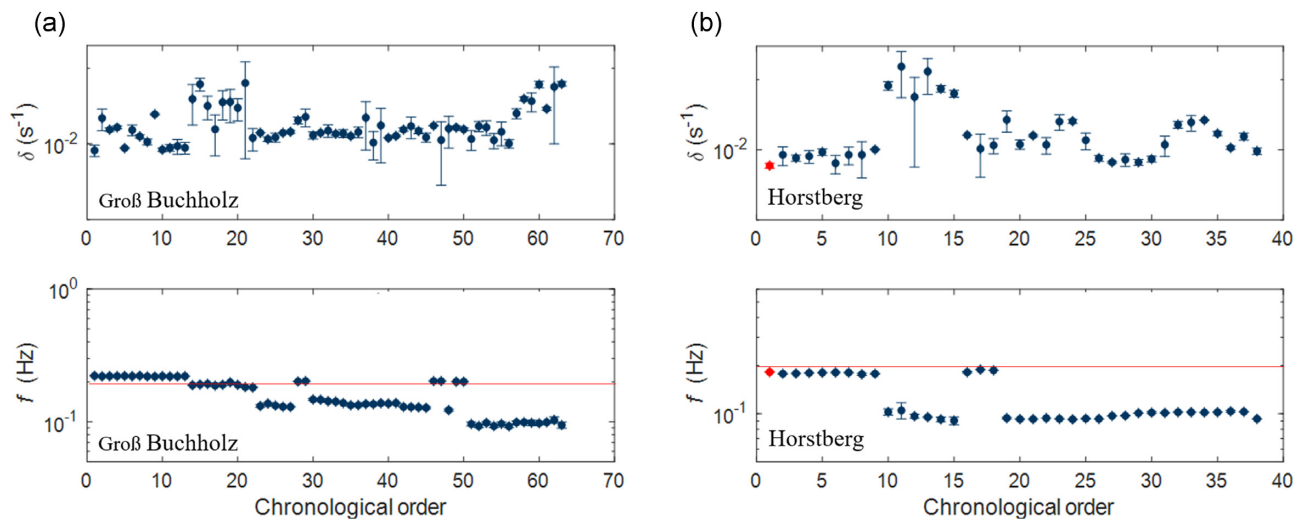


Figure 6. Damping coefficient (top) and frequency (bottom) of the free pressure oscillations observed for boreholes (a) Groß Buchholz and (b) Horstberg during pumping operations as a function in their chronological order. The red data point denotes the observation during the pulse test in borehole Horstberg. The frequencies of oscillations depend on borehole mean pressures. The nominal eigenfrequency $\hat{f}_0 = c_0/(2L)$, indicated in a horizontal red line, for both boreholes with a length of 4000 m is 0.19 Hz.

of the boreholes, of 2 m length (3902.5–3926.6 m) in Volpriehausen and 4 m length (3787–3791 m) in Detfurth formation for Horstberg, and 2 m length (3707–3709 m) in Volpriehausen formation for Groß Buchholz. The casing radius and thus the radius of the injection sections is 0.18 m for both, but the radius of the inner liner is 0.1 m for Horstberg and 0.18 m for Groß Buchholz.

4.1.1.2 KTB The KTB main hole (Hauptbohrung) is located in Windischeschenbach, Bavaria, Germany. The borehole penetrates paragneisses, orthogneisses, and metabasic rocks (Emmermann & Lauterjung 1997). The cased section of the borehole has a length of 9030 m and the radius of the inner injection liner was 0.14 m. The open-hole section has a nominal radius of 0.18 m and a length of 70 m between 9030 m and the final depth of 9100 m. At the start of the hydraulic testing, a pulse test was carried out to assess the integrity of the inner liner when it was still closed by a burst disc at its lower end. After the disc was brought to failure, several hydraulic fracturing tests were performed in the open-hole section followed by 5 pulse tests during which the pressure response exhibited oscillatory behaviour.

4.1.2 Results

4.1.2.1 Groß Buchholz and Horstberg During the pumping operations in borehole GT1 (Groß Buchholz), the early oscillations (1 to 13) exhibited frequencies of about 0.22 Hz close to the Nyquist frequency of the recording (Table 5). After the injection of a large fluid volume, during which the pressure critical for opening pre-existing fractures of 35 MPa was exceeded (Fischer 2016), the frequencies started decaying slightly (Fig. 6a). Further injection and production cycles and the second stimulation enlarged the fracture area (Pechan *et al.* 2014, 2015) and in their wake, the fracture apparently lost its ability to close fully even at borehole pressures below the nominal opening pressure. The oscillations during this phase showed a continuous decrease in their frequencies from 0.13 Hz (oscillations 19 to 48 in Fig. 6a) to 0.10 Hz (oscillations 49 to 63 in Fig. 6a). The damping coefficient slightly increased towards the end of the operations (Fig. 6a top).

In the Horstberg borehole, free oscillations were recorded when injecting in either the Volpriehausen (oscillations 1–18) or the Detfurth (oscillations 19–37) formation. The set of oscillations recorded during pulse tests in the Volpriehausen formation exhibits frequencies around 0.18 Hz and 0.10 Hz at borehole pressures below and above the opening pressure of about 42 MPa (Gerling *et al.* 2015), respectively (Fig. 6b). Frequencies of oscillations also ranged around 0.1 Hz during the stimulation operations carried out in the Detfurth formation (Fig. 6a top) at injection pressures between 20 and 30 MPa that sufficed to open existing fractures and create new ones (Gerling *et al.* 2015). The damping coefficients range between 0.009 and 0.025 s⁻¹, the higher values associated with the lower frequencies around 0.1 Hz (Fig. 6b).

The frequencies of the free pressure oscillations recorded in Horstberg and Groß Buchholz, when the present fractures were presumably closed or at least partially closed, are close to the eigenfrequency $\hat{f}_0 \sim 0.19$ Hz of a tube with a length of 4000 m and two closed ends (Figs 7a and b). The damping coefficients associated with these frequencies are between 2 and 10 times higher than the limit posed by (1) for Groß Buchholz (Fig. 7a), while the deviation is less than a factor of 2 for Horstberg (Fig. 7b). In contrast, the damping coefficients associated with frequencies around 0.1 Hz, observed when fractures were presumably open, exceed the tight-borehole damping coefficient by 20 to 30 times for Groß Buchholz and Horstberg (Figs 7a and b). Therefore, we inverted only these latter pairs of frequency and damping coefficient for hydraulic properties using the model for leaky boreholes (2).

The spectral components suitable for hydraulic analysis give effective permeabilities of $\sim 10^{-17}$ to $\sim 10^{-13}$ m² for either borehole, unaffected by varying apparent porosity from 1×10^{-2} to 1×10^{-1} (Fig. 8a). These effective permeabilities correspond to effective fracture

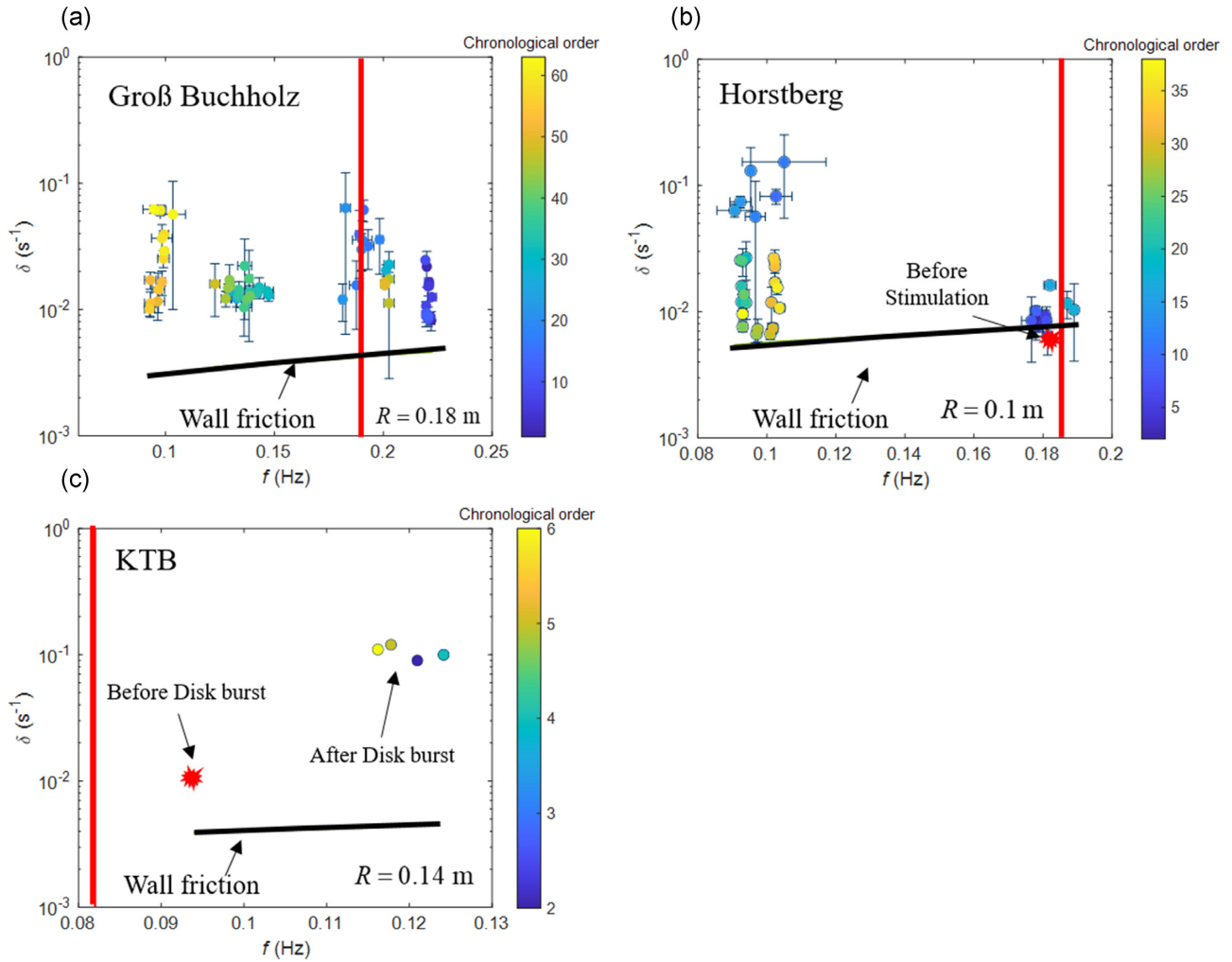


Figure 7. Comparison of damping coefficients and frequencies from free oscillations observed for (a) Groß Buchholz, (b) Horstberg and (c) KTB with wall friction given by (1), using the radii indicated in the plots. Red data point denotes the pulse test in Horstberg and the sealing test in KTB before stimulation. Colouring indicates the temporal evolution of the spectral components of the pressure oscillations. The vertical red lines indicate the nominal eigenfrequencies of the boreholes.

apertures of $\sim 10^{-5}$ to $\sim 10^{-4}$ m using the relations given in (3) for both axial and radial fractures, matching the effective fracture aperture of about $\sim 10^{-4}$ m calculated from the fracture transmissibility values reported by Pechan *et al.* (2015) for Groß Buchholz. The wide range of permeability seems to reflect its pressure dependence (Fig. 8b and c). Pressure increased by 45 MPa with progressing pumping for Groß Buchholz (Fig. 8b), but decreased by 25 MPa for Horstberg (Fig. 8c). The sensitivity of permeability to fluid pressure can be represented by the permeability modulus $K_k = \partial p_f / \partial \ln k$ (Yilmaz *et al.* 1994), a small value of K_k indicating a strong dependence of permeability on fluid pressure. The apparent permeability modulus deduced from using the borehole pressure, an upper bound for the fluid pressure in the tested fractures, ranges between 3.5 and 10 MPa and between 15 and 85 MPa for Horstberg and Groß Buchholz, respectively (Fig. 8c). While our approach likely overestimates the true permeability moduli, because we used changes in the borehole pressure that likely exceed changes in the fluid pressure along the fracture, the gained values are comparable to permeability moduli of fractured Bunter sandstone reported by Hernandez Castañeda (2020) and of different types of fractured rocks reported by Kranz *et al.* (1979) and Raven & Gale (1985).

Previous spectral analysis of free pressure oscillations in Groß Buchholz GT1 using Weidler's (1996) model yielded a decrease in transmissivity during the course of the stimulation (Fischer 2016). This result is not only counterintuitive since transmissivity values should increase during hydraulic stimulation as a consequence of the creation of new fractures and/or the shearing of pre-existing ones but also at conflict with the independent conventional analyses of observed pressure transients (Pechan *et al.* 2015). In the light of the derived analytical solution (2), the increase in damping coefficient observed in the course of the stimulation (Fig. 7a) indicates that transmissivity has actually increased, i.e. our treatment resolves the problems apparently associated with the oscillation analysis. The decrease in permeability over the course of pumping operations in Horstberg is likely due to the coeval decrease in mean injection pressure (Fig. 8c).

4.1.2.2 KTB The free oscillation that occurred, when the burst disc was still intact in the KTB main hole, had a frequency in agreement with the eigenfrequency $\hat{f}_0 \sim 0.086$ Hz of a 9030 m long tube with both ends closed. The damping coefficient for this oscillation is about two times

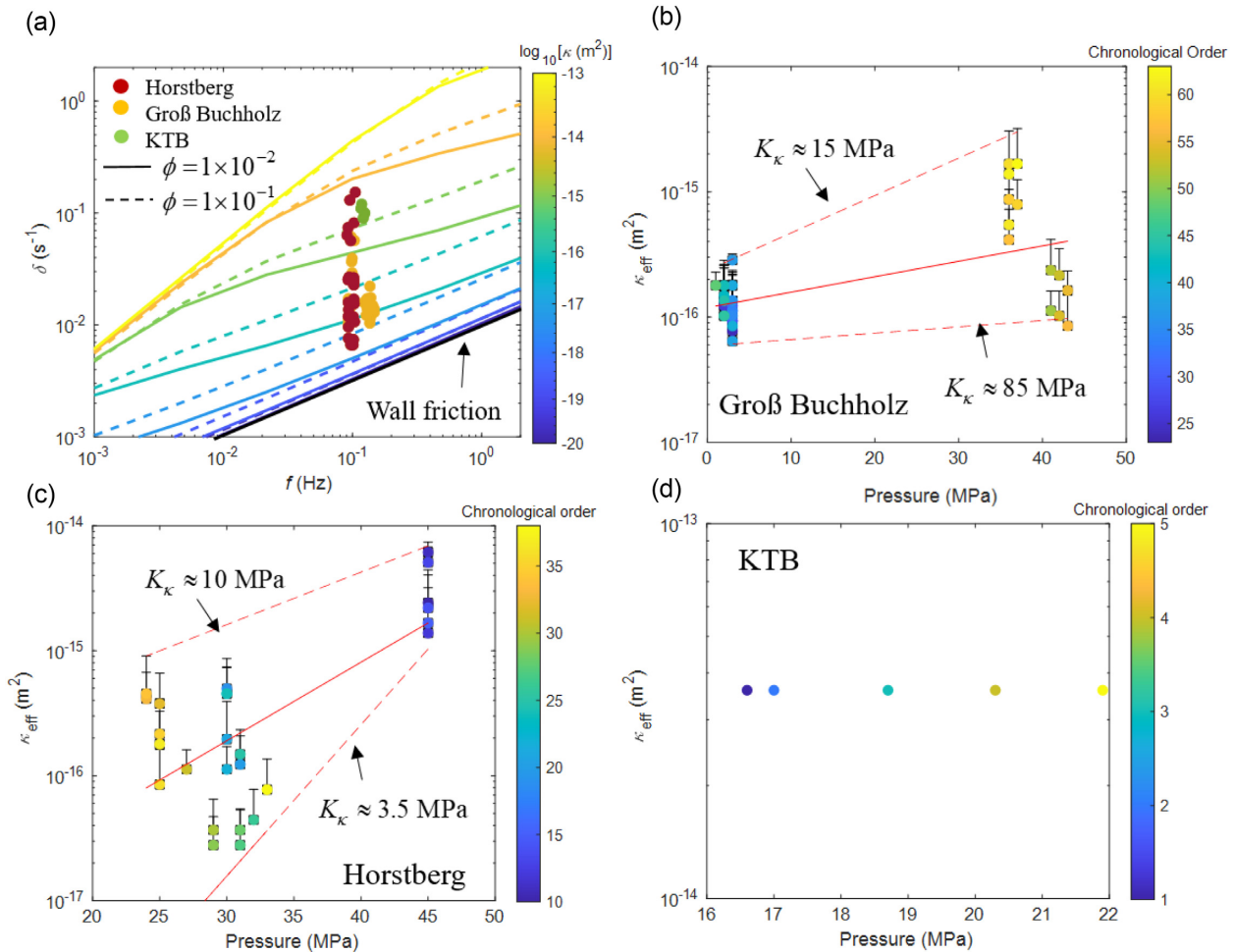


Figure 8. (a) Comparison of damping coefficients and frequencies from the observed free oscillations in Groß Buchholz, Horstberg and KTB with the theoretical predictions for leaky boreholes (2), using the indicated effective permeability (colour bar) and apparent porosity. Effective permeabilities as a function of mean interval pressure during oscillations and chronological order of appearance (colour bar) for (b) Groß Buchholz, (c) Horstberg and (d) KTB. Red lines represent the linear relation $\ln(\kappa) = \ln(\kappa_0) + \Delta P/K_k$, where κ_0 is the permeability at zero pressure and K_k denotes the permeability modulus.

the value of the theoretical prediction for a tight and rigid system (Fig. 7c). The oscillations recorded after the inner liner was connected to the open-hole section exhibited higher frequencies and ten times higher damping coefficients values than observed before (Fig. 7c). Contrary to the observed increase in frequency, the increase in length of the hydraulic system associated with the removal of the burst disk should result in a minor decrease in frequency. The increase in damping coefficient beyond that given by (1) suggests that leakage into the metamorphic rock rather than wall friction controls pressure wave attenuation after removal of the burst disk.

The characteristics of the free pressure oscillations that occurred during pumping operations after the disk failure correspond to effective permeabilities of about 10^{-14} m² according to (2), see Fig. 8(d). The effective permeability does neither increase with the progression of the pumping nor with the modest increase of injection pressure by ~ 5 MPa (Fig. 8d). Shapiro *et al.* (1997) estimated a permeability of $\sim 10^{-16}$ m² from the growth of the cloud of induced seismic events, assuming an effective storage capacity of $\sim 10^{-14}$ Pa⁻¹. The value for the storage capacity used by Shapiro *et al.* (1997) is two orders of magnitude lower than the value assumed for our analysis, i.e. $\phi/K_f = 4 \times 10^{-12}$ Pa⁻¹, corresponding to an apparent porosity $\phi = 1 \times 10^{-2}$. For the specific storage capacity used by Shapiro *et al.* (1997), i.e. using $s_{\text{eff}} = 5 \times 10^{-14}$ Pa⁻¹, the predictions by (2) shift downwards leading to an increase in permeability obtained from the free oscillations and thus an even larger difference to the estimate reported by Shapiro *et al.* (1997). Using the relations given in (3), an effective permeability of 10^{-14} m² corresponds to fracture apertures of 0.2 or 1 mm for a pair of axial fractures (assuming $L_f = 70$ m) or a radial fracture, respectively. The comparison of results is not without problems since the analyses by Shapiro *et al.* (1997) is indirect. However, differences between the estimates for permeability may reflect scale-dependence of permeability (e.g. Song & Renner 2006; Boutt *et al.* 2012; Kinoshita & Saffer 2018), since free-pressure oscillations are associated with a penetration depth $r_p \sim \sqrt{\kappa_{\text{eff}}/(\mu_f s_{\text{eff}} f_0)}$ of about 5 m, while the observed seismic cloud covers distances from the borehole beyond ~ 100 m.

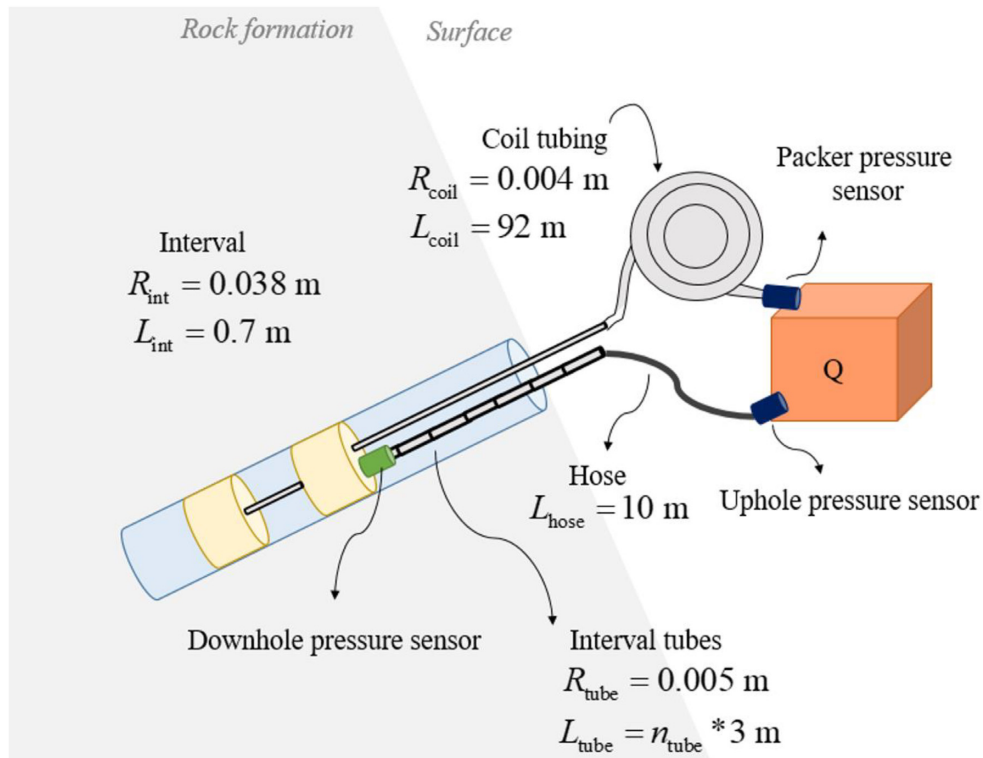


Figure 9. Sketch (not to scale) of the set up used during the stimulation protocols in the injection borehole in the mine Reiche Zeche, Freiberg, Germany. In the calibration experiment, the borehole was modelled by a steel pipe of 4 m length. The total length of the injection line, L_{tube} , depends on the number of tubes, n_{tube} , used, each with 3 m length. We used $n_{\text{tube}} = 10$ for the calibration experiment.

4.2 Double-packer intervals

Experiments with the double-packer probe of Solexperts GmbH, Bochum, Germany, were carried out in boreholes in Freiberg, Germany, and Hong Kong, China, and in a steel tube in the course of a calibration test. The probe consisted of two inflatable packers isolating an interval of 0.7 m length connected to the pump at the surface by straight tubes in Freiberg and by a coiled tubing in Hong Kong. At either site, the packers were connected to the pump by a coiled tubing. The interval pressure was measured with an uphole sensor as well as a downhole sensor (Fig. 9) whereas a single uphole sensor was used for the packer pressure. During field tests and calibration tests, free oscillations were excited when the pump valve was rapidly opened or closed.

4.2.1 Field equipment and site description

4.2.1.1 Calibration experiment A calibration experiment was conducted with the probe inserted in a steel tube with a radius of 0.038 m and an injection line comprised of 10 steel tubes with 3 m length and 5 mm inner radius, consistent with the field set up in Freiberg. Pressures were recorded with a sampling rate of 20 Hz.

4.2.1.2 Reiche Zeche, Freiberg As part of the STIMTEC project (Renner *et al.* 2020; Jiménez Martínez & Renner 2021; Boese *et al.* 2022), stimulation tests were performed in a 63 m long borehole with a radius of 0.038 m dipping 15° downwards starting from a horizontal tunnel in the research mine Reiche Zeche in Freiberg, Saxony, Germany. The penetrated rock is a gneiss. Ten intervals were successively isolated by the double-packer probe and connected to the pump by a 10 m long hose and an injection line of steel tubes of 3 m length and 5 mm inner radius. The number of tubes used increased from 11 to 16 with increasing depth. Signals of the three pressure sensors (Fig. 9) were recorded with a sampling rate of 5 and 20 Hz during the field tests of intervals deeper than 33.1 m and at 28.1 m, respectively.

4.2.1.3 Hong Kong Hydraulic fracturing tests were performed in a vertical borehole (BH-CAV108) with a length of 279.68 m and a radius of 0.038 m penetrating granite in Sha Tin, Hong Kong (Gerd Klee 2018, personal communication). Ten test intervals of 0.7 m length were selected at different depths. The injection line was a coiled tubing of 300 m length with a radius of 0.004 m. Signals of the downhole pressure sensor were recorded with a sampling rate of 5 Hz.

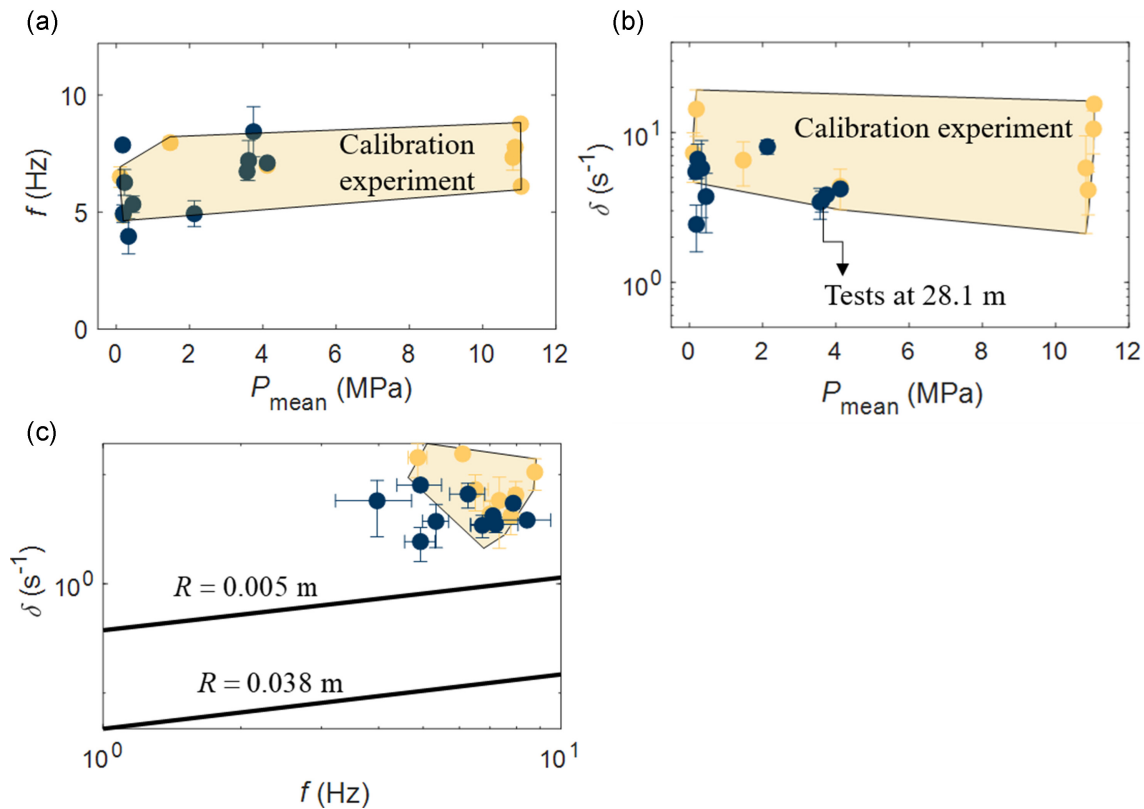


Figure 10. Spectral components from the calibration experiment for the set up used in Freiberg calculated using Prony analysis (yellow data points and their representation by the yellow shadowed areas). Spectral components for oscillations observed for the interval at 28.1 m in borehole BH10, Reiche Zeche, Freiberg. (a) Frequency and (b) damping coefficient as a function of mean interval pressure. (c) Damping coefficient vs. frequency for the oscillations from the interval at 28.1 m in comparison with the theoretical damping from wall friction using the indicated radii representing the injection tubes (0.005 m) and the interval (0.038 m).

4.2.2 Results

4.2.2.1 Calibration experiment During the calibration experiment, we recorded 13 oscillations in interval pressure by the uphole and downhole sensors, and 16 oscillations in packer pressure. The latter had a frequency of $f_0 = 3.9 \pm 0.3$ Hz, in close agreement with the theoretical prediction of $f_0 = 4.0$ Hz for a standing wave in a tube with one open-end and the length of the coiled tubing connected to the packers, 92 m. The packer volume is two times the tubing volume and thus apparently acts similar to a constant-pressure boundary characterizing an open end, see Appendix F.

The interval-pressure oscillations exhibited frequencies varying from 5 to 10 Hz (Fig. 10a). Neither frequency nor associated damping coefficients seem to vary systematically with mean interval pressure (Figs 10a and b). The variability in frequency and damping coefficient may arise from turbulence in the flow due to the tube fittings (Fig. 9). For a standing wave in a 40 m long tube (10 tubes of 3 m length and the hose of 10 m length), one open end should give an eigenfrequency of 9 Hz whereas two closed ends give 18 Hz. The interval and the injection line have similar volumes of about 3 litres and therefore the end condition is difficult to predict. Furthermore, the frequencies of the recorded oscillations might be affected by aliasing since the eigenfrequency of 18 Hz of a tube with two closed ends surpasses the Nyquist frequency of 10 Hz, i.e. the observed frequencies could be apparent and low compared to the real eigenfrequencies of the system.

4.2.2.2 Reiche Zeche, Freiberg In the field campaign at Reiche Zeche, 30 free oscillations occurred during pumping operations in the intervals at 28.1, 33.9, 37.9 and 49.7 m. For the last three intervals, free oscillations took place when the interval was depressurized, i.e. when the interval was briefly vented to air pressure (Fig. 11a). This venting process induces a backflow from the pressurized fluid in the fracture(s) to the interval at low pressure. The frequencies of these oscillations around 1 Hz differ from the range observed in the calibration test, that is 5–10 Hz, already potentially underestimated due to aliasing, even after accounting for the difference in tube length. Such a significant deviation from the fundamental frequency is at odds with the numerical results that revealed small reductions in frequencies of free pressure oscillations for leaky sections (see Appendix D). We thus suspect that the determined frequency values are affected by aliasing. For a sampling rate of 5 Hz, the nominal eigenfrequency of 9 Hz (assuming one open end) will be recorded as an oscillation with an apparent frequency of 1 Hz (Penny *et al.* 2003).

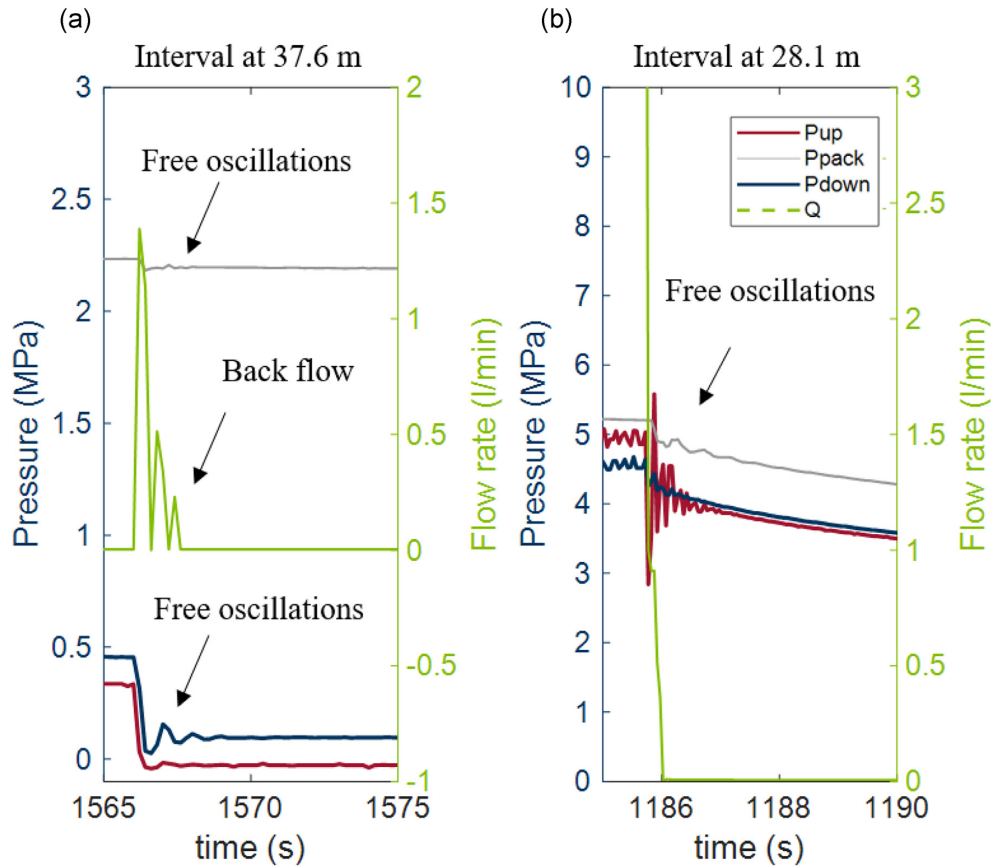


Figure 11. Examples of free oscillations recorded in the intervals at (a) 37.9 m, associated with a back-flow test (Q denotes flow rate) during a shut-in phase, and at (b) 28.1 m, associated with initial shut-in, in Reiche Zeche, Freiberg. The pressure recorded by the uphole sensor (P_{up}) shows a higher amplitude than that at the downhole sensor (P_{down}) for the interval at 28.1 m; the opposite is true for the interval at 37.6 m. Oscillations are also recorded by the sensor connected to the packer line (P_{pack}).

The frequencies of the oscillations for the interval at 28.1 m lie in the range of the frequencies recorded in the calibration experiment (Fig. 10a). These frequencies are more reliable than the oscillation frequencies from the other intervals since a higher sampling frequency (20 Hz) was used, i.e. sufficient for one open-end (9 Hz). These oscillations took place during changes in flow rate at elevated pressure (Fig. 11b). The majority of their spectral components lie in the range of those of the calibration experiment (Figs 10a and b) but above the analytical curve of wall friction of the tubes with a radius of 0.005 m. The effect of wall friction associated with the borehole wall comprising the interval with a radius of 0.038 m is negligible. For the hydraulic analysis, we consider only the oscillations with spectral components lying outside the range covered by the calibration data (Fig. 10c).

The observed damping exceeds that of the coiled tubing alone indicating a contribution by leakage in the interval (Fig. 10c). Because our model does not account for changes in radius, we invert the spectral parameters using the dispersion relation for full-length leaky boreholes (2) with the interval radius. The transmissivity values of the borehole range between 10^{-10} to 10^{-7} $\text{m}^2 \text{s}^{-1}$ using an apparent porosity of $\phi = 1 \times 10^{-2}$ and a total injection length of 41 m (Table 5). These transmissivity values likely represent overestimations because of the damping in the narrow tube, yet they compare well with the range of transmissivities obtained from periodic pumping tests (PPT) performed with periods ranging from 40 to 900 s at different interval mean pressures after stimulation (Jimenez Martinez 2020).

4.2.2.3 Hong Kong Free oscillations were recorded by the downhole pressure sensor during the tests in Hong Kong for all intervals. The analysis of the spectral components revealed frequency values around 1.25 Hz (Fig. 12), coinciding with the nominal eigenfrequency for one open end (Table 5). The volume of the interval of about 3 litres is five times lower than the volume of the injection line, thus here the interval probably constitutes a closed-end-condition; yet, the oscillations occurred during a change in the flow rate (non-zero) before the valve is closed, which may result in an open-end condition for the inlet of the tubing. The damping coefficients range between the predictions for viscous damping of flow waves in rigid (1) and elastic pipes (using eq. 46 in Bernabé 2009), see Fig. 12. Thus, the oscillations seem to reflect wall friction in the long narrow coiled tubing that is not perfectly rigid.

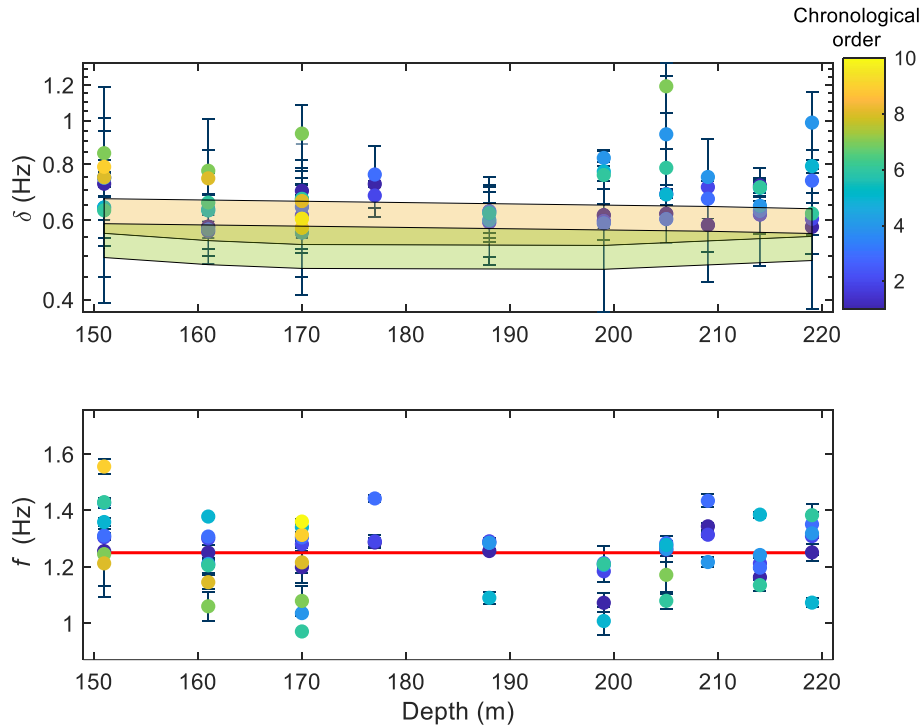


Figure 12. Spectral components of free oscillations observed after stimulation in borehole BH-CAV108, Hong Kong. Top: Comparison of the observed damping coefficients with the predicted damping from wall friction (calculated using the observed frequency range) for a rigid (green shaded area) and an elastic pipe (yellow shaded area, $V_s = 3000$ m/s) with a radius of 0.004 m, i.e. that of the injection line. Bottom: Comparison of the observed frequencies with the eigenfrequency of a pipe with a length of 300 m and one open end (red line).

5 DISCUSSION

5.1 Usefulness of free pressure oscillation for hydraulic analyses

The fundamental benchmark for the usefulness of observed free oscillations for hydraulic analyses is the frequency-damping coefficient relation for a tight borehole. The numerical results confirm the fundamental applicability of the analytical model of Bernabé (2009), although it was derived neglecting advective terms in the Navier–Stokes equation and the continuity equation, and nonlinear terms due to the fluid compressibility in the Navier–Stokes equation. Thus, the analytical model can be used as a diagnostic tool for the dominance of wall friction, as applies to the field study in Hong Kong. Only when observed damping coefficients exceed those associated with the attenuation of a flow wave due to wall friction a meaningful hydraulic analysis is possible. Then, it is still necessary to discriminate whether factors such as rock deformability, turbulence, etc. may account for variable and/or large damping coefficients relative to the predictions of (1). For typical porous medium-shear moduli of 10 GPa, corresponding to a shear wave velocity $V_s \sim 2000$ m s⁻¹, or more, the effect of rock deformability on the damping coefficient is less than 10 per cent (Fig. 12). Yet, the elasticity of pipes with finite thickness, not treated by the model, enhances the effective deformability, i.e. it reduces the effective stiffness of the material, and may give rise to further dissipative wave modes (e.g. Kurzeja *et al.* 2016). Non-ideal borehole geometries, i.e. variable casing diameter or changing orientation (e.g. Groß Buchholz), and pipe connections (e.g. in Freiberg set-up), might cause turbulence during steady or pulsatile flow (Najjari & Plesniak 2018) and thus increase the damping coefficient in comparison to (1). Using damping coefficients increased by turbulence or other effects in (2) leads to an overestimation of the inverted effective permeability.

Avoiding aliasing problems when recording free-pressure oscillations requires sampling rates that exceed the typical values used during hydraulic testing of boreholes. The resolution of the acquisition tool should be adjusted to at least capture the expected fundamental frequency of the system. For example, instead of 2 Hz, Audouin & Bodin (2007) should have used a sampling frequency, higher than 6 or 12 Hz to capture the fundamental frequency of the 130 m long borehole for both ends closed or one open, respectively.

The free pressure oscillations can be inverted using (2) when the fluid flow in the porous medium or the fractures is governed by viscous forces. An extension of the boundary condition of the radial velocity to account for flow beyond a purely diffusive process, i.e. account for the inertia effects on the flow in the conduits, is possible using the theory of ‘dynamic permeability’ for a homogenous porous medium (Johnson *et al.* 1987) or a radial fracture (Tang *et al.* 1989). The critical frequency $\omega_c = \mu_f / (\rho_f R_p^2)$ discriminates whether inertia effects are relevant; for a conduit with a characteristic size R_p (Biot 1956), viscous effects are dominant when $\omega \ll \omega_c$. For the frequencies in our observations ranging from 10⁻² to 10⁰ s⁻¹ to fall in the inertia-controlled regime, the characteristic conduit size had to exceed $R_p > 10^{-3}$ m by large (as is true for the injection tubes and boreholes). When fractures are opened during stimulation they may reach apertures close to this

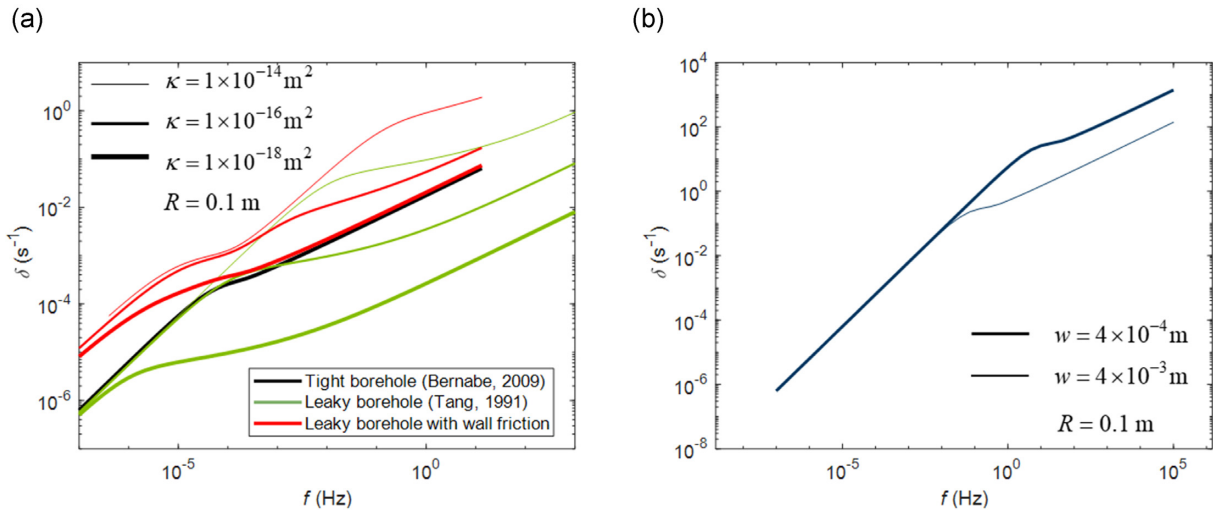


Figure 13. (a) Comparison of damping coefficient and frequency from dispersion relations for fluid flow waves in tight boreholes (1), in leaky boreholes accounting for (2) and neglecting wall friction (Tang *et al.* 1991b). (b) Damping coefficient and frequency from the dispersion relation for fluid flow in a radial fracture (Tang *et al.* 1989) with the two indicated apertures.

order of magnitude and a treatment involving ‘dynamic permeability’ may have to be considered. Yet, realistic homogeneous porous media (e.g. Nishiyama & Yokoyama 2017) and fractures below reopening pressure do not exhibit pore sizes or apertures in this range, respectively. Thus, we infer that the conventional diffusion approach (2) will typically suffice for an evaluation of spectral characteristics of free pressure oscillations.

5.2 Comparison of dispersion relations for waves in leaky boreholes

The derived dispersion relation (2) for flow waves in leaky boreholes with rigid walls that includes viscous losses by wall friction applies for flow waves with any frequency. The frequencies of the standing waves analysed here are relatively low compared to frequencies, for which the actual propagation of flow waves can be observed. Frameworks focusing on the propagative character are the classical theory of Stoneley waves in permeable (Tang *et al.* 1991b; Ou & Wang 2019) and fractured boreholes (Tang & Cheng 1989; Tang *et al.* 1991a), and the recently presented ‘selective resonance for radial fractures’ (Liang *et al.* 2017). The dispersion relation of Stoneley waves in an axially fractured borehole, somewhat inconsistently, employs the dispersion relation derived for a radial fracture to describe the leakage contribution (Tang & Cheng 1989). The analytical dispersion relations for Stoneley waves in permeable boreholes account for the effect of viscous forces on the fluid flow in the porous medium (or the fractures) but neglect the effect of the viscous interaction of the fluid and the borehole wall and, in contrast to our solution for leaky boreholes (2), give damping coefficients below the tight-borehole limit regardless of frequency (Fig. 13a). Thus, care must be taken when using the dispersion relations for Stoneley waves to derive hydraulic parameters from propagating waves (e.g. Tang *et al.* 1991b) when the damping coefficients are below the tight borehole limit.

For a borehole intersected by a radial fracture, only transmission and reflection coefficients were determined (Tang & Cheng 1989; Tang 1990). Liang *et al.* (2017) considered a situation where the disruption of the borehole constituted by a radial fracture governs the oscillation behaviour of the entire system. Then, the damping coefficient and the frequency of the fluid-flow wave in the borehole may be governed by the dispersion relation for the fluid wave in the radial fracture (e.g. Tang & Cheng 1989). The presence of a radial fracture in a borehole might lead to a pressure node and thus to an increase in frequency comparable to the effect of holes in flutes (Wolfe *et al.* 2001). The dispersion relation for fluid-flow waves in a radial fracture (Tang & Cheng 1989; Liang *et al.* 2017) yields a decrease in damping with increasing aperture (Fig. 13b), physically plausible considering the fracture alone. For the system ‘borehole–fracture’, however, increasing aperture corresponds to an increase in leakage that in turn should manifest in increasing damping, as true for the dispersion relation for leaky boreholes (2). Obviously, the coupling condition between fracture and borehole deserves further attention.

6 CONCLUSIONS

We derived a dispersion relation for flow waves in boreholes penetrating permeable media, assessed it by complementary numerical simulations, and used it to constrain hydraulic properties from an analysis of the spectral characteristics of free pressure oscillations recorded during hydraulic tests. The flow-wave dispersion relation presented in this work is an extension of the solution for tight boreholes by an account for leakage into hydraulic conduits at the borehole wall, albeit strictly true only for homogeneous media due to the imposed radial symmetry and the underlying fluid-volume balancing between borehole and intersected hydraulic conduits. The current version of the extended dispersion relation restricts to the dominance of viscous forces for the pressure propagation in the porous medium, in accord with the range of actually

observed frequencies, but an extension towards dynamic permeability is possible. Objectives for future work lie in addressing changes in borehole radius and deviations of the flow field in the borehole from radial symmetry associated with leakage into fractures.

The dispersion relations for infinitely long boreholes do not constrain the frequency at which a standing fluid-flow wave oscillates. Our numerical simulations for boreholes with finite length showed that length is the dominant factor for frequency; irrespective of whether the borehole is tight, fully or partial leaky, the conventional organ-pipe relations apply apart from frequency reductions due to damping, by leakage or wall friction.

The determination of hydraulic properties using the derived analytical solution is limited towards the low end by permeability around $\sim 10^{-18}$ m² for typical borehole radii between 0.038 and 0.18 m. This limitation in resolution reflects that leakoff is just one of at least two dissipation processes. The numerical results demonstrate that the free oscillations can be overdamped for a typical borehole radius when permeability values are around $\sim 10^{-13}$ m². However, when the wall friction contribution is high, i.e. for a borehole with small radius, overdamping can occur at lower permeabilities than that value. Thus, the window of permeability values that can be inverted from free pressure oscillations comprises about 5 order of magnitudes. The inverted permeabilities constitute effective values, representative of the borehole's transmissivity, whose conversion toward real permeability values requires knowledge of the length of the leaky sections or of details of the fracture geometry.

The hydraulic tests of various field campaigns were performed with set-ups including double-packer intervals and cased wells with perforation or open-hole sections. The oscillations recorded in these tests exhibited frequencies and damping coefficients varying from 10^{-2} to 10^0 Hz and 10^{-3} to 5×10^0 s⁻¹, respectively. The observed frequencies were in good agreement with the nominal eigenfrequency of waves in tubes with corresponding length and end condition. The damping coefficients from numerical simulations and field campaigns were always similar to or higher than the analytical limit defined by wall friction in a tight borehole. Thus, this limit allows for the identification of the physical processes controlling the oscillations, that is viscous losses between the fluid and the borehole wall or fluid flow from the borehole to the porous medium. Effective permeability values inverted from the proposed dispersion relation for leaky boreholes fall in a plausible range between 10^{-18} and 10^{-14} m². In particular, the use of coiled tubings might be problematic since it causes significant wall friction, whose contribution may thus dominate the damping coefficient. For shallow boreholes, the eigenfrequency of the free pressure oscillations might be higher than the Nyquist frequency of the data-acquisition systems typically used for hydraulic tests, leading to aliasing problems.

The strength of the proposed method lies in the simplicity of monitoring a single perturbation of flow and recording for tens of seconds the pressure response with sufficient sampling frequency. Changes in damping coefficients in the course of a stimulation operation are a strong indication that the corresponding oscillations actually bear information on hydraulic properties of the penetrated formation. In these cases, the 'incidental' data from free pressure oscillations provide 'real-time' evidence for fracture evolution during stimulation tests. Likewise, they can provide constraints on the dependence of hydraulic parameters on mean fluid pressure. The presented workflow could as well be applied to the evaluation of hydraulic properties of underdamped oscillations in slug tests.

ACKNOWLEDGMENTS

The authors gratefully acknowledge the funding provided by the German Federal Ministry of Education and Research (BMBF) for the STIMTEC project (subprojects HYSPALAB and SPATZ, Grant numbers 03A0015A and 03G0901A). We are grateful to Gerd Klee from SolExpert (Bochum) who performed field and calibration tests for the data in Freiberg and Hong Kong. Dr Torsten Tischner from BGR (Hannover) is in particular thanked for providing the data for the boreholes Groß Buchholz 1 and Horstberg. We are grateful for the constructive and helpful feedback from two anonymous reviewers.

DATA AVAILABILITY

The spectral parameters of the simulated pressure oscillations are available in the paper. The spectral parameters of oscillations recorded in the field are available in tabular form in the PhD thesis entitled 'Hydraulic Changes induced by Stimulation' by Victoria Jimenez Martinez (2020) published by Ruhr-Universität Bochum, University Library at <https://doi.org/10.13154/294-7815>.

REFERENCES

- Audouin, O. & Bodin, J., 2007. Analysis of slug-tests with high-frequency oscillations, *J. Hydrol.*, **334**, 282–289.
- Bernabé, Y., 2009. Oscillating flow of a compressible fluid through deformable pipes and pipe networks: wave propagation phenomena, *Pure appl. Geophys.*, **166**, 969–994.
- Biot, M.A., 1956. Theory of propagation of elastic waves in a fluid-saturated porous solid II. Higher frequency range, *J. acoust. Soc. Am.*, **28**, 179–191.
- Boese, C.M., Kwiatek, G., Fischer, T., Plenkers, K., Starke, J., Blümle, F., Janssen, C. & Dresen, G., 2022. Seismic monitoring of the STIMTEC hydraulic stimulation experiment in anisotropic metamorphic gneiss, *Solid Earth*, **13**, 323–346.
- Boutt, D.F. *et al.*, 2012. Scale dependence of in-situ permeability measurements in the Nankai accretionary prism: the role of fractures, *Geophys. Res. Lett.*, **39**, 2–7.
- Bredehoeft, J.D., 1967. Response of well aquifer systems to earth tides, *J. geophys. Res.*, **72**, 3076–3087.
- Bredehoeft, J.D., Cooper, H.H. & Papadopoulos, I.S., 1966. Inertial and storage effects in well-aquifer systems: an analog investigation, *Water Resour. Res.*, **2**, 697–707.
- Chadwick, P. & Borejko, P., 1994. Existence and uniqueness of Stoneley waves, *Geophys. J. Int.*, **118**, 279–284.
- Cheng, Y. & Renner, J., 2018. Exploratory use of periodic pumping tests for hydraulic characterization of faults, *Geophys. J. Int.*, **212**, 543–565.

- Dziewonski, A., Bloch, S. & Landisman, M., 1969. A technique for the analysis of transient seismic signals, *Bull. seism. Soc. Am.*, **59**, 427–444.
- Emmermann, R. & Lauterjung, J., 1997. The German continental deep drilling program (KTDB), *J. Geophys. Res.*, **102**, 18 179–18 201.
- Fischer, G. & Paterson, M., 1992. Measurement of permeability and storage capacity in rocks during deformation at high temperature and pressure, in *Fault Mechanics and Transport Properties of Rocks, International Geophysics Series*, pp. 213–252, eds Evans, B. & Wong, T.F., Academic Press.
- Fischer, J., 2015. Approximation of slightly compressible fluids by the incompressible Navier–Stokes equation and linearized acoustics: a posteriori estimates, 1–32.
- Fischer, L.L., 2016. Auswertung von freien Druckschwingungen in Bohrlöcheruntersuchen und erzwungenen Druckschwingungen in Laboruntersuchen zur Bestimmung hydraulischer Eigenschaften. *PhD thesis*, Ruhr-Universität Bochum.
- Forster, C., 2010. *Musical Mathematics: On the Art and Science of Acoustic Instruments*, Chronicle Books, pp. 227–248.
- Frizell, J.P., 1898. Pressures resulting from changes of velocity of water in pipes, *Trans. ASCE*, **39**, 1–18.
- Georgi, H., 2015. *The Physics of Waves*, Prentice Hall.
- Gerling, J.P., Tischner, T., Kosinowski, M. & Bräuer, V., 2015. Erdwärmegewinnung mittels Generierter geothermischer Systeme (GeneSys), *Geol. Jahrb. R. A*, **162**, 261.
- Guiltinan, E. & Becker, M.W., 2015. Measuring well hydraulic connectivity in fractured bedrock using periodic slug tests, *J. Hydrol.*, **521**, 100–107.
- Halliday, D., Resnick, R. & Walker, J., 2011. *Fundamentals of Physics*, 9th edn, John Wiley & Sons, Inc.
- Hernandez Castañeda, M.C., 2020. Investigation into the evolution of hydraulic properties of fractured rocks at conditions representative of deep geothermal reservoirs, Ruhr-Universität Bochum.
- Hsieh, P.A., Bredehoeft, J.D. & Farr, J.M., 1987. Determination of aquifer transmissivity from Earth tide analysis, *Water Resour. Res.*, **23**, 1824–1832.
- Hubbert, M. & Willis, D.G., 1957. Mechanics of hydraulic fracturing, *Trans. AIME*, **210**, 153–168.
- Jimenez Martinez, V.A., 2020. Hydraulic changes induced by stimulation. *PhD thesis*, Ruhr-Universität Bochum, doi:10.13154/294-7815.
- Jiménez Martínez, V.A. & Renner, J., 2021. Injectivity Enhancement of Freiberg Gneiss by Hydraulic Stimulation, in *55th U.S. Rock Mechanics/Geomechanics Symposium*, June 18–25.
- Johnson, D.L., Koplik, J. & Dashen, R., 1987. Theory of dynamic permeability and tortuosity in fluid saturated porous media, *J. Fluid Mech.*, **176**, 379–402.
- Kinoshita, C. & Saffer, D.M., 2018. In situ permeability and scale dependence of an active accretionary prism determined from cross-borehole experiments, *Geophys. Res. Lett.*, **45**, 6935–6943.
- Kipp, K.L.J., 1985. Type curve analysis of inertial effects in the response of a well to a slug test, *Water Resour. Res.*, **21**, 1397–1408.
- Korneev, V., 2010. Low-frequency fluid waves in fractures and pipes, *Geophysics*, **75**, N97–N107.
- Kranz, R.L., Frankel, A.D., Engelder, T. & Scholz, C.H., 1979. The permeability of whole and jointed Barre Granite, *Int. J. Rock Mech. Min. Sci.*, **16**, 225–234.
- Krauss, I., 1974. Die Bestimmung der Transmissivität von Grundwasserleitern aus dem Einschwingverhalten des Brunnen-Grundwasserleitersystems, *J. Geophys.*, **40**, 381–400.
- Kreiss, H.O., Lorenz, J. & Naughton, M.J., 1991. Convergence of the solutions of the compressible to the solutions of the incompressible Navier–Stokes equations, *Adv. Appl. Math.*, **12**, 187–214.
- Kurzeja, P., Steeb, H., Strutz, M.A. & Renner, J., 2016. Oscillatory fluid flow in deformable tubes: implications for pore-scale hydromechanics from comparing experimental observations with theoretical predictions, *J. acoust. Soc. Am.*, **140**, 4378–4395.
- Lai, G., Ge, H. & Wang, W., 2013. Transfer functions of the well-aquifer systems response to atmospheric loading and Earth tide from low to high-frequency band, *J. geophys. Res.*, **118**, 1904–1924.
- Liang, C., O'Reilly, O., Dunham, E.M. & Moos, D., 2017. Hydraulic fracture diagnostics from Krauklis-wave resonance and tube-wave reflections, *Geophysics*, **82**, D171–D186.
- Lobos, T., Reziner, J. & Schegner, P., 2003. Parameter estimation of distorted signals using Prony method, *IEEE Bologna Power Tech Conference Proceedings*. Bologna, Italy, doi:10.1109/PTC.2003.1304801.
- Mcelwee, C.D. & Zenner, M.A., 1998. A nonlinear model for analysis of slug-test data, *Water Resour. Res.*, **34**, 55–66.
- Najjari, M.R. & Plesniak, M.W., 2018. Secondary flow vortical structures in a 180 elastic curved vessel with torsion under steady and pulsatile inflow conditions, *Phys. Rev. Fluids*, **3**, 1–21.
- Nishiyama, N. & Yokoyama, T., 2017. Permeability of porous media: role of the critical pore size, *J. geophys. Res.*, **122**, 6955–6971.
- Ou, W. & Wang, Z., 2019. Simulation of Stoneley wave reflection from porous formation in borehole using FDTD method, *Geophys. J. Int.*, **217**, 2081–2096.
- Pechan, E., Tischner, T. & Renner, J., 2014. Fracture properties after hydraulic stimulation in low-permeability sediments (GeneSys-project), *Rock Eng. Rock Mech. Struct. Rock Masses - Proc. EUROCK 2014, ISRM Eur. Reg. Symp.* 1397–1402. doi:10.1201/b16955-243.
- Pechan, E., Tischner, T. & Renner, J., 2015. Evidence for a highly conductive fracture after water fracturing in the GeneSys project, *Int. J. Geomech.*, **16**, 04015081.
- Penny, J.E.T., Friswell, M.I. & Garvey, S.D., 2003. Detecting aliased frequency components in discrete fourier transforms, *Mech. Syst. Signal Process.*, **17**, 473–481.
- Rasmussen, T.C., Haborak, K.G. & Young, M.H., 2003. Estimating aquifer hydraulic properties using sinusoidal pumping at the Savannah River site, South Carolina, USA, *Hydrogeol. J.*, **11**, 466–482.
- Raven, K.G. & Gale, J.E., 1985. Water flow in a natural rock fracture as a function of stress and sample size, *Int. J. Rock Mech. Min. Sci.*, **22**, 251–261.
- Renner, J., Adero, B., Becker, F., Blümle, F., Boese, C. M., Cheng, Y., Dresen, G., Fischer, T., Frühwirth, T., Janssen, C. et al., 2020. STIMTEC: a mine-scale hydraulic stimulation experiment of anisotropic metamorphic rock with evaluation by mine-back drilling, *American Rock Mechanics Association Letters*. Winter 2021, 30, 2–4.
- Renner, J. & Messar, M., 2006. Periodic pumping tests, *Geophys. J. Int.*, **167**, 479–493.
- Saar, M.O. & Manga, M., 2003. Seismicity induced by seasonal groundwater recharge at Mt. Hood, Oregon, *Earth planet. Sci. Lett.*, **214**, 605–618.
- Schep, L.L. & Renner, J., 2021. Evidence for the heterogeneity of the pore structure of rocks from comparing the results of various techniques for measuring hydraulic properties, *Transp. Porous Media*, **136**, 217–243.
- Shapiro, S. A., Huenges, E. & Borm, G., 1997. Estimating the crust permeability from fluid-injection-induced seismic emission at the KTB site, *Geophys. J. Int.*, **131**(2), 15–18.
- Song, I. & Renner, J., 2006. Experimental investigation into the scale dependence of fluid transport in heterogeneous rocks, *Pure appl. Geophys.*, **163**, 2103–2123.
- Tang, X., Cheng, C.H. & Toksöz, M.N., 1989. Stoneley wave propagation in a fluid-filled borehole with a vertical fracture, *1989 SEG Annu. Meet.*, pp. 30–32. doi:10.1190/1.1889737.
- Tang, X.M., 1990. Acoustic logging methods in fractured and porous formations. *PhD thesis*, Massachusetts Institute of Technology, USA. doi:10.4172/2472-0518.1000139.
- Tang, X.M. & Cheng, C.H., 1989. A dynamic model for fluid flow in open borehole fractures, *J. geophys. Res.*, **94**, 7567–7576.
- Tang, X.M., Cheng, C.H. & Paillet, F.L., 1991a. Modeling borehole Stoneley wave propagation across permeable in-situ fractures, in , Society of Professional Well Log Analysts, Midland, TX.
- Tang, X.M., Cheng, C.H. & Toksöz, M.N., 1991b. Dynamic permeability and borehole Stoneley waves: a simplified Biot-Rosenbaum model, *J. acoust. Soc. Am.*, **90**, 1632–1646.
- van der Kamp, G., 1976. Determining aquifer transmissivity by means of well response tests: the underdamped case, *Water Resour. Res.*, **12**.

Weidler, R.-T., 1996. Ein Verfahren zur Bestimmung hydraulischer Kenngrößen aus dem Schwingungsverhalten eines abgeschlossenen Bohrloch-Riß Systems. *Diploma thesis*, Ruhr-Universität Bochum.

Wolfe, J., Smith, J., Tann, J. & Fletcher, N.H., 2001. Acoustic impedance spectra of classical and modern flutes, *J. Sound Vib.*, **243**, 127–144.

Yilmaz, Ö., Nolen-Hoeksema, R.C. & Nur, A., 1994. Pore pressure profiles in fractured and compliant rocks, *Geophys. Prospect.*, **42**, 693–714.

Zimmerman, R. W. & Bodvarsson, G. S., 1996. Hydraulic conductivity of rock fractures, *Transport in Porous Media*, **23**, 1–30. doi:10.1007/BF00145263.

APPENDIX A

A.1 Relation between damping and dispersion relations

A pressure wave propagating in the negative z -direction is described by

$$p_w(z, t) = P_0 e^{i(\omega t + kz)}, \quad (4)$$

where P_0 is the amplitude, k is the wavenumber and ω is the angular frequency, related to the wave velocity, c , by $k = \omega/c$. Introducing a complex-valued wave number $k_z = k_{\text{Re}} + ik_{\text{Im}}$, with real, k_{Re} , and imaginary part, k_{Im} , gives

$$p_w(z, t) = p_0 e^{-k_{\text{Im}} z} e^{i(k_{\text{Re}} z - \omega t)}, \quad (5)$$

that is propagation is controlled by the real part yielding an effective propagation velocity $c_{\text{eff}} = \omega/k_{\text{Re}}$, and the damping, that is the amplitude reduction with travelled distance, is controlled by the imaginary part corresponding directly to the spatial damping coefficient $\delta^* = k_{\text{Im}}$.

For intrinsic attenuation, that is energy loss related to a uniform material property such that every local oscillation behaves as its neighbours, the damping for a travel distance of one wavelength is identical to the local damping during one period T_0 , and thus

$$e^{-\delta^* \lambda} = e^{-\delta T_0} \quad (6)$$

giving the relation

$$\delta = \delta^* \frac{\lambda}{T_0} = k_{\text{Im}} c_{\text{eff}} = \omega \frac{k_{\text{Im}}}{k_{\text{Re}}} \quad (7)$$

between the two measures of damping, δ^* (m^{-1}) and δ (s^{-1}).

APPENDIX B

B.1 Dispersion relation for fluid flow waves in leaky boreholes

We seek wave-like solutions of the continuity and the Navier–Stokes equation for the fluid pressure in the borehole, $p_w(r, z, t)$, and the fluid velocity, which comprises an axial, $u(r, z, t)$ and a radial, $v(r, z, t)$ component:

$$p_w(r, z, t) = P_w(r) e^{-i(\omega t - zk_z)}, \quad (8)$$

$$u(r, z, t) = U(r) e^{-i(\omega t - zk_z)}, \quad \text{and} \quad (9)$$

$$v(r, z, t) = V(r) e^{-i(\omega t - zk_z)}, \quad (10)$$

where r and z denote the radial and axial coordinates, respectively, and t is the time. In the long-wavelength approximation, the amplitudes $P_w(r)$, $V(r)$ and $U(r)$, found by Bernabé (2009), are

$$P_w(r) = P_0, \quad (11)$$

$$U(r) = C(\omega) J_0(\sqrt{2i}r/v) + \frac{P_0 k_z}{\rho_f \omega}, \quad \text{and} \quad (12)$$

$$V(r) = -C(\omega) \frac{\sqrt{2i} \mu_f}{v \rho_f \omega} k_z J_1(\sqrt{2i}r/v) + \frac{P_0}{v^2} i \mu_f r \frac{\omega^2 - c_0^2 k_z^2}{\rho_f^2 \omega^2 c_0^2}, \quad (13)$$

where the amplitude of the pressure wave is P_0 and

$$C(\omega) = -\frac{P_0}{\rho_f \omega J_0(\sqrt{2i}R/v)} k_z(\omega) \quad (14)$$

is found by requiring the axial fluid velocity (12) to be zero at the solid–fluid interface ($r = R$). These amplitudes represent general solutions still valid when assuming a boundary condition at the borehole wall different from the one employed by Bernabé (2009). Unlike for the dispersion relation for tight boreholes (1) that results from imposing the radial fluid velocity to be zero at the solid–fluid interface, we define

a leakage condition for the radial velocity component using Darcy's law, that is

$$V(R) = -\frac{\kappa_{\text{eff}}}{\mu_f} \frac{\partial p_f}{\partial r}, \quad (15)$$

where p_f is the fluid pressure in the rock penetrated by the borehole and κ_{eff} the rock's effective permeability, identical to the intrinsic or Darcy permeability for a homogeneous porous medium.

We assume that the fluid pressure in the porous medium exhibits the same wave-like character as the borehole pressure (8), that is

$$p_f(r, z, t) = P_f(r) e^{-i(\omega t - zkz)} \quad (16)$$

with an amplitude $P_f(r \geq R)$ depending on radial distance from the borehole. Laminar, uncoupled, purely radial flow in the porous medium is described by a diffusion equation

$$\frac{\partial p_f}{\partial r^2} + \frac{1}{r} \frac{\partial p_f}{\partial r} + \frac{\partial^2 p_f}{\partial z^2} = \frac{1}{D} \frac{\partial p_f}{\partial t}, \quad (17)$$

with the hydraulic diffusivity of the medium, $D = \kappa_{\text{eff}} / (\mu_f s_{\text{eff}})$, which comprises the effective specific storage capacity s_{eff} of the rock penetrated by the borehole. The hydraulic diffusivity determines how far a pressure perturbation reaches into a permeable medium in a specific time. Inserting ansatz (16) in (17) gives the ordinary differential equation

$$\frac{dP_f}{dr^2} + \frac{1}{r} \frac{dP_f}{dr} + \left(k_z^2 - \frac{i\omega}{D}\right) P_f = 0 \quad (18)$$

with the general solution

$$P_f(r) = MI_0\left(r\sqrt{k_z^2 - \frac{i\omega}{D}}\right) + NK_0\left(r\sqrt{k_z^2 - \frac{i\omega}{D}}\right) \quad (19)$$

involving the modified Bessel functions of zero order of first $I_0(\cdot)$ and second kind $K_0(\cdot)$ and constant unknown factors M and N . Assuming the permeable porous medium to have an infinite radial extension on the timescale of the perturbation, the fluid pressure obeys $P_f(r \rightarrow \infty) \rightarrow 0$ requiring $M = 0$. The continuity in pressure at the borehole wall,

$$P_f(R) = P_w(R) = P_0, \quad (20)$$

constrains the second constant N leading to

$$P_f(r) = P_0 \frac{K_0\left(r\sqrt{k_z^2 - \frac{i\omega}{D}}\right)}{K_0\left(R\sqrt{k_z^2 - \frac{i\omega}{D}}\right)}. \quad (21)$$

The result for the fluid pressure in the porous medium (21) can be used to calculate the radial fluid velocity at the borehole wall using Darcy's law (15)

$$V(r = R) = -\frac{\kappa_{\text{eff}}}{\mu_f} P_0 \sqrt{k_z^2 - \frac{i\omega}{D}} \frac{K_1\left(R\sqrt{k_z^2 - \frac{i\omega}{D}}\right)}{K_0\left(R\sqrt{k_z^2 - \frac{i\omega}{D}}\right)}, \quad (22)$$

where $K_1(\cdot)$ denotes the modified Bessel function of second kind and first order. Finally, equating (13) for $r = R$ to (22), the dispersion relation of a fluid-flow wave experiencing wall friction in a leaky borehole is implicitly given by (2).

For a homogeneous permeable medium, the radial velocity (15) of the borehole fluid is identical to the Darcy velocity in the rock and the effective permeability is identical to the intrinsic or Darcy permeability, $\kappa_{\text{eff}} = \kappa$. Heterogeneity, that is variations in hydraulic properties along the borehole, perturbs the velocity field in the borehole. We simplify the evaluation of the boundary condition (15) by solely accounting for the 'averaged' effect of fractures or open-hole sections on the volume balance between them and the borehole at $r = R$:

$$A_w V(r = R) = -A_{F,\text{ohs}} \frac{\kappa_{F,\text{ohs}}}{\mu_f} \frac{\partial p_f}{\partial r} \Big|_{r=R}, \quad (23)$$

where $A_w = 2\pi RL$ denotes the area of the borehole with length L , $A_{F,\text{ohs}}$ and $\kappa_{F,\text{ohs}}$ represent the cross-sectional area and permeability of the fracture(s) or the permeable open-hole section. For partial leakage into a homogeneous open-hole section, the cross-sectional area is $A_{\text{ohs}} = 2\pi RL_{\text{leaky}}$, with the length of the permeable section L_{leaky} , and (23) yields

$$V(R) = -\frac{L_{\text{leaky}}}{L} \frac{\kappa}{\mu_f} \frac{\partial p_f}{\partial r} \Big|_{r=R}. \quad (24)$$

We assume the cubic law to hold for fractures, i.e. the fracture permeability relates to aperture as $\kappa_F = w^2/12$ (e.g. Zimmerman and Bodvarsson 1996). For our simplistic averaging (23) that ignores the actual deviations of flow lines in the borehole from a radial direction, two diametrically opposite axial fractures, as for example created by hydraulic fracturing (Hubbert & Willis 1957), of aperture w and length

L_F , that is $A_{F,ax} = 2wL_F$, give

$$V_{F,ax}(R) = -\frac{w^3 L_F}{12\pi R L \mu_f} \left. \frac{\partial p_f}{\partial r} \right|_{r=R}, \quad (25)$$

and a single radial fracture, that is $A_{F,rad} = 2\pi R w$, gives

$$V_{F,rad}(R) = -\frac{w^3}{12L \mu_f} \left. \frac{\partial p_f}{\partial r} \right|_{r=R}. \quad (26)$$

APPENDIX C

C.1 Signal Processing and Spectral analysis

Pairs of frequency and damping coefficient were gained from decomposing observed oscillations into their spectral components. Extracting the fundamental mode was performed by three signal-processing methods, that is Prony analysis (PA), fast Fourier transformation (FFT) and multiple-filter-technic (MFT). Prony analysis is a method for estimating spectral components of a signal by modelling sampled data as a linear combination of exponential functions (Lobos *et al.* 2003). The application of this method requires selecting the order (number of exponentials). The multiple-filter technic is a method for analyzing multimode dispersed signals utilizing Fourier transformation for successive sections of the signal, that is employing moving windows. The method yields amplitudes and phases as a function of frequency (Dziewonski *et al.* 1969) and constrains the persistence of frequency components through the duration of a signal.

For the field tests, we performed the spectral analysis on pressures recorded by the sensors installed uphole (data from Horstberg, Groß Buchholz, KTB and Freiberg) and/or downhole (data from Freiberg and Hong Kong); for the numerical simulations, we employed pressures recorded at the center of the boreholes at half their heights. Processing of the pressure records consisted of two steps. In the first step, we used FFT and/or MFT to retrieve an estimate of the dominant frequency of the oscillation. Then, we selected the oscillatory contribution, characterized by frequency and damping coefficient, identified by Prony analysis corresponding to the dominant frequency obtained in the first step. The uncertainty of the spectral components was calculated from changes in the spectral components associated with varying the order, that is the number of exponential functions used to fit the signal, during the Prony analysis.

APPENDIX D

D.1 Models

The numerical simulations were performed with the software COMSOL Multiphysics, a commercial finite element solver for partial differential equations, here the Navier–Stokes equations for a compressible fluid including advective inertia terms, neglected in the derivation of (1) and (2), and assuming the Stokes condition for bulk viscosity, that is the fluid's compressibility β_f is constant. Fluid compressibility was prescribed through a pressure-dependent density according to

$$\rho = \rho_f (1 + \beta_f p). \quad (27)$$

We used parameters corresponding to water in the simulations (Table 1).

All simulated boreholes were embedded in a rigid solid, and had an open top and a closed bottom. For the tight model, the borehole lengths (L) were 1, 4, 8, 100, 400 and 1000 m, while we restricted to 4, 100 and 400 m for the full-length leaky and partial-length leaky models. The permeable section of partial-length leaky boreholes was located at the end of the well with a height spanning between 0.1 and 80 per cent of the entire length of the borehole. The axial 'no-slip boundary' was uniformly applied. The walls of tight boreholes corresponded to a no-flow boundary also for the radial direction. For leaky boreholes, fluid flow from the borehole into the porous medium was specified by the boundary condition (15) for the radial velocity component at the borehole wall. This boundary condition was the source term for the radial pressure diffusion into the isotropic porous medium following (18). We considered permeability values between 10^{-18} and 10^{-13} m². The leaky boreholes had a fixed apparent porosity of $\phi_{app} = 1\%$, corresponding to a specific storage capacity of $s \simeq 4.2 \times 10^{-12}$ Pa⁻¹. Thus, diffusivity differences between simulations are solely controlled by permeability.

We used a range of meshes whose element size was controlled by the automatic meshing generator of COMSOL. The combination of polynomial orders of the interpolation functions (P_v and P_p) for the velocity (v) and pressure (p) field affects the characteristics of numerical free pressure oscillations. For two polynomials of first order ($P1_v + P1_p$), only tested for tight boreholes, the damping coefficients exceed those gained for two polynomials of second order ($P2_v + P2_p$) and those predicted by the analytical solution (1), see Fig. D4c. However, we found no difference in spectral components when selecting a polynomial of second order for the velocity and either taking a polynomial of first or second order for the pressure field (Table 4). Thus, in view of computational efficiency, we used interpolation functions of the type ($P2_v + P1_p$).

Velocity and pressure were set to zero at the initial time. The pressure perturbation was realized by a rapid impulse prescribed at the top of the water column using a step function with a height of 1 Pa and a rise time of $\sim 1/f_0$, where $f_0 \sim c_0/4L$ represents the nominal

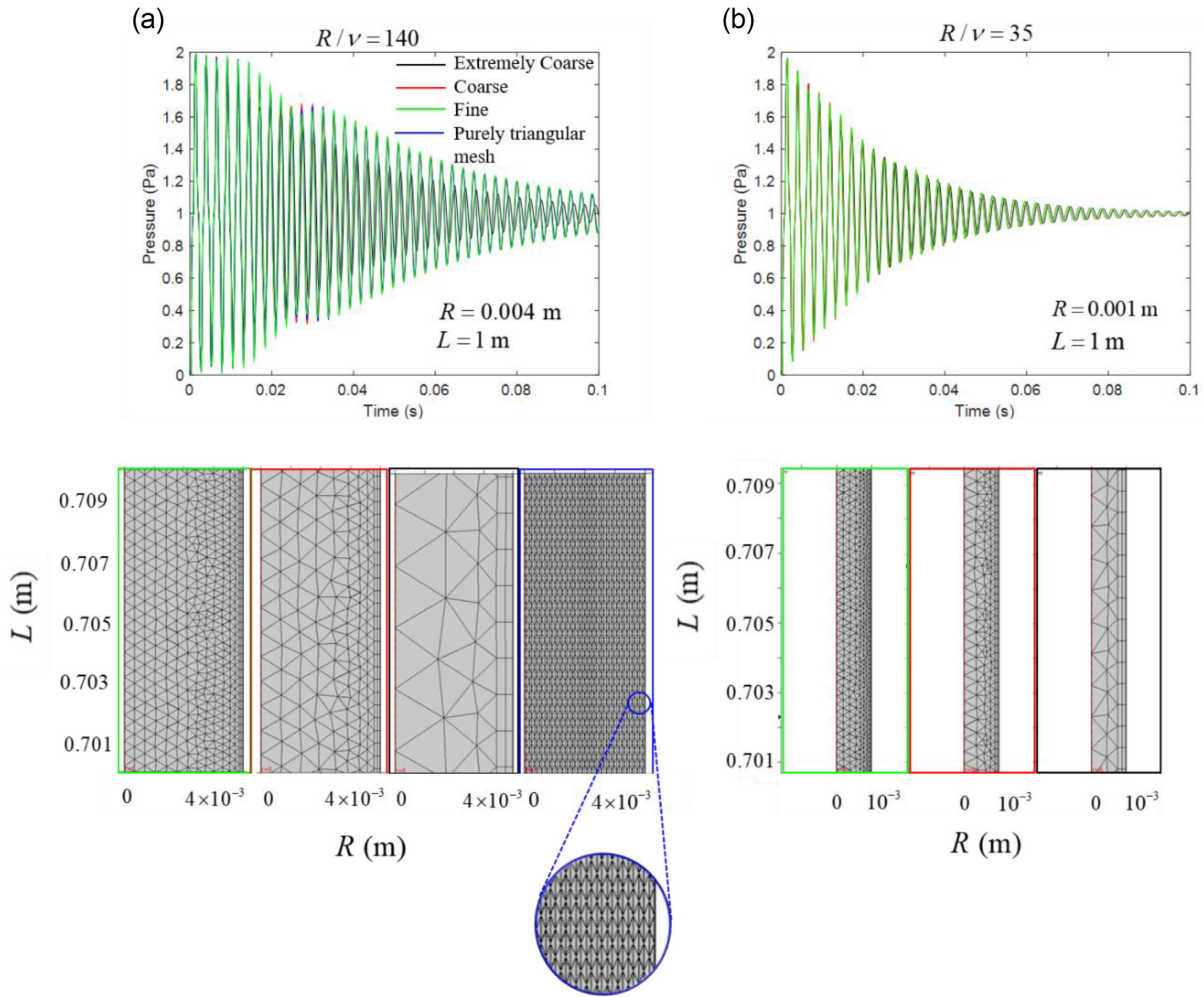


Figure D1. Effect of mesh size on the free pressure oscillations in tight boreholes (length 1 m) for two different ratios of borehole radius to viscous skin depth. The extremely coarse (black), coarse (red) and fine (green) meshes have two types of elements (rectangular at the borehole wall and triangular everywhere else) with varying size. The purely triangular mesh (blue) is composed of uniform triangles.

eigenfrequency of a tight borehole of length L with one open end. Eigenfrequencies of $f_0 \sim 387, 96, 48, 3.8, 0.96,$ and 0.38 Hz correspond to the modelled lengths of $L = 1, 4, 8, 100, 400,$ and 1000 m, respectively. The radius of the tight boreholes ranged from 0.4 mm to 0.1 m and from 0.01 m to 0.18 m for the leaky boreholes. In all simulations, the viscous skin depth associated with the fundamental frequency of the excited fluid-flow waves is one to three orders of magnitude smaller than the radii of the boreholes.

D.2 Effect of mesh density on spectral components of pressure oscillations

We varied the mesh type and size in a suite of simulations for two boreholes with the same length of 1 m but radii of 0.001 and 0.004 m, corresponding to $R/\nu = 35$ and 140 , respectively, where the viscous skin depth is calculated using the fundamental frequency. The first type of mesh consisted of triangular elements in the interior of the borehole and rectangular elements close to the borehole wall; the size of the elements for this type of mesh becomes finer towards the borehole wall (Fig. D1). The second type of mesh consisted of triangular elements with uniform size throughout. For either type, the element size is controlled in COMSOL by an automatic meshing generator. For the first type, it offers categories from ‘extremely coarse’ to ‘extremely fine’; for the second type, the automatically chosen size of the triangular elements can be reduced by a scale factor.

The radial length of the first element close to the borehole wall r_e changed from 3×10^{-5} to 2.5×10^{-4} m for both considered mesh types (Table 6). The pressure records exhibit significant mesh-dependence for the borehole with the large radius but less so for the borehole with the small radius (Fig. D1, Table 6). For both borehole radii and all mesh sizes and types, the frequencies deduced by spectral analysis, however, match with the conventional fundamental frequency and the harmonics for a borehole with one open end, $f_m = (2m + 1)f_0$; the harmonics to order three deviate by less than 3 per cent from the odd multiples of the fundamental frequency (Fig. D2a).

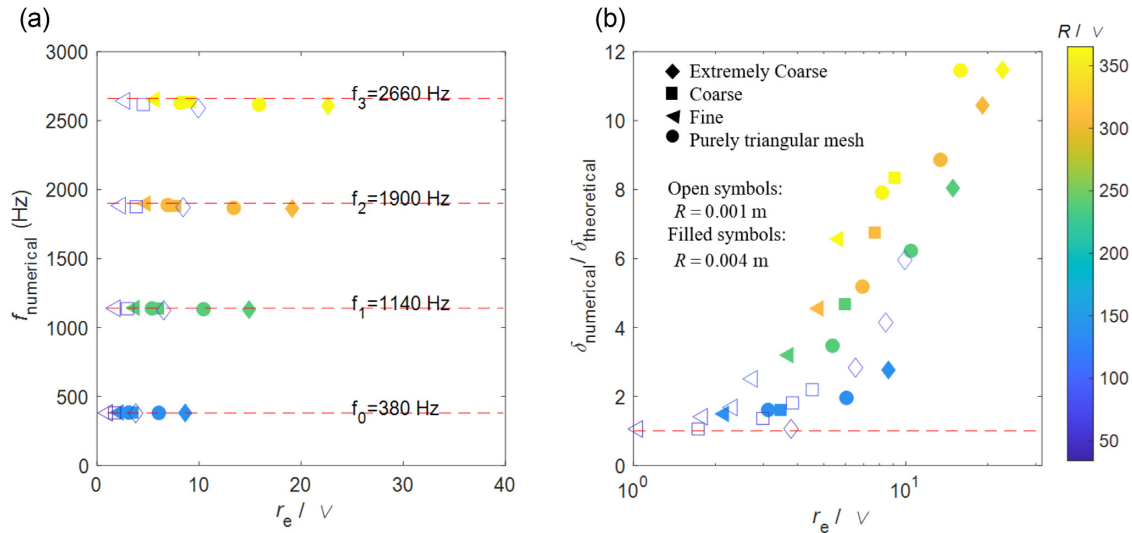


Figure D2. (a) Fundamental frequency and associated harmonics, and (b) damping coefficients normalized by the theoretical damping coefficient given by (1) as a function of the ratio of the radius of the first mesh element close to the borehole wall (r_e) to viscous skin depth (ν) from free pressure oscillations simulated with different mesh type and element size for boreholes with a length of 1 m and radii of 0.001 and 0.004 m. The colour bar represents the ratio of the radius of the borehole to the viscous skin depth. In a), dashed red lines indicate the nominal frequencies of standing waves in a borehole with one open end; in b), the dashed red line indicates consistency between theory and numerical modelling.

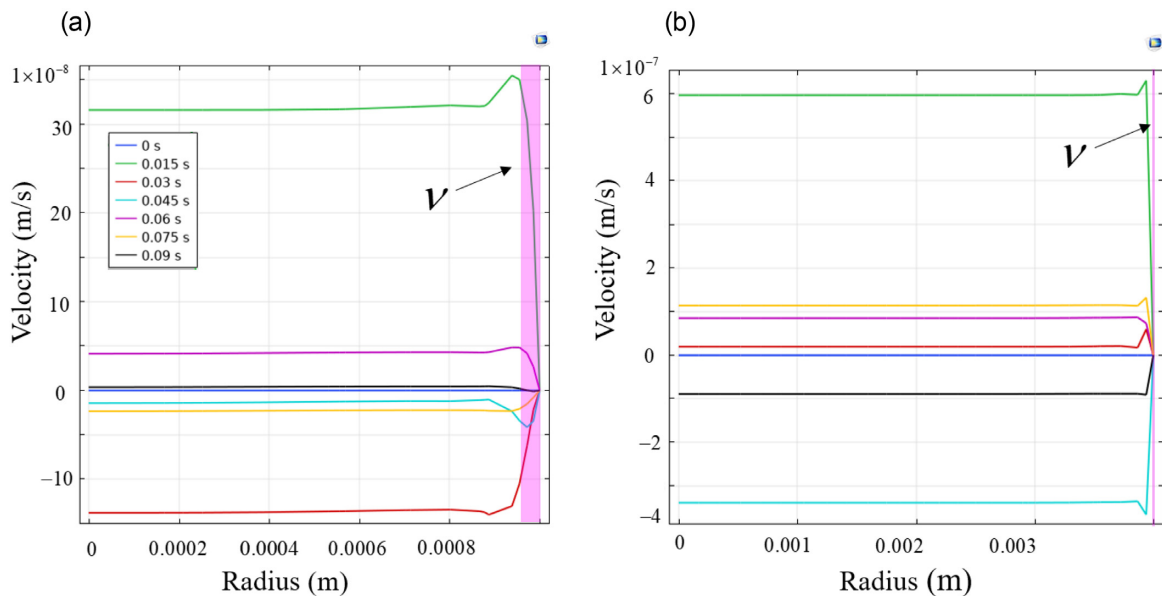


Figure D3. Variation in axial velocity distribution over the course of damped oscillations with a fundamental frequency of 380 Hz (period of about 0.0026 s) for a borehole with 1 m length and (a) $R = 0.001$ m and (b) $R = 0.004$ m using a fine mesh (automatically generated by COMSOL). The extension of the viscous skin depth of $\nu = 2.9 \times 10^{-5}$ m is represented in magenta colour.

The overestimation of the numerical damping coefficients in comparison to the analytical solution is dominated by the ratio r_e / ν but is independent of the type of element close to the borehole wall, i.e. triangular or rectangular. The ratio of the numerical damping coefficient of the fundamental mode and the harmonics to the theoretical predictions given by (1) tends to one when the radial extension of the element closest to the borehole wall does not significantly exceed the viscous skin depth, i.e. $r_e / \nu \sim 1$ (Fig. D2b). For a fixed r_e , the ratio of r_e / ν is higher for viscous skin depth associated to the harmonics than to the fundamental mode, therefore, the numerical damping coefficient harmonics significantly differ from the analytical prediction. The overestimation in damping coefficient is also affected by the ratio R / ν likely reflecting that not only the size of the element nearest to the borehole wall but the size of all elements changes with absolute borehole radius (Fig. D2b).

The radial velocity profile is expected to be piston-like when viscous skin depths are much smaller than the borehole radius (e.g. Kurzeja *et al.* 2016). The associated steep velocity decline towards the borehole wall was well resolved for a small borehole radius of 0.001 m, as indicated by its variability during an oscillation period (Fig. D3a). In contrast, the velocity profiles in a borehole with a four times larger

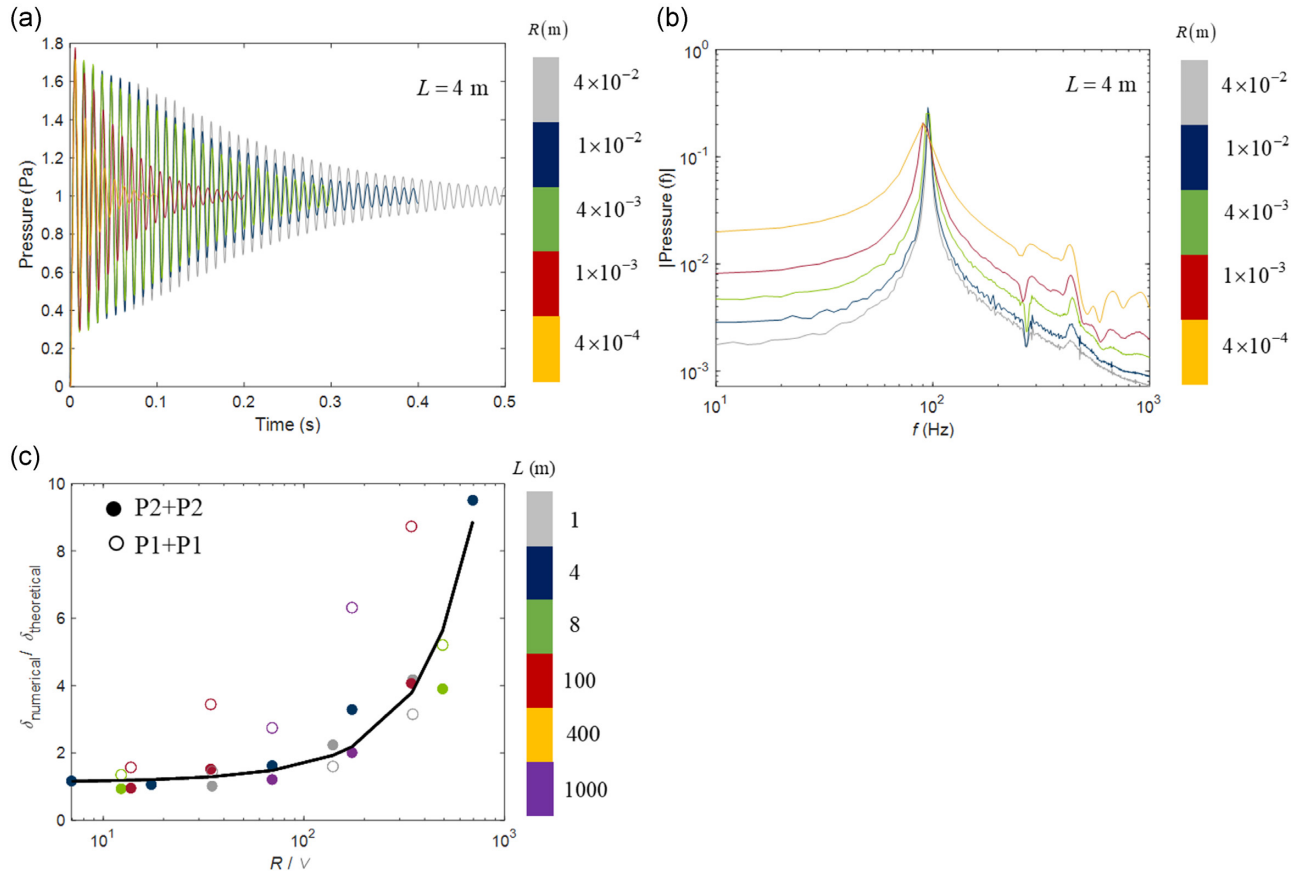


Figure D4. Pressure oscillations resulting from numerical simulations for tight boreholes with a length of 4 m and radii as indicated by the colour bar: (a) time-series; (b) amplitude spectrum. (c) Comparison of the damping coefficients from numerical modelling, that is using the polynomial interpolating functions $P2_v + P2_p$ and $P1_v + P1_p$, and analytical solution as a function of the ratio of the borehole radius and viscous skin depth for tight boreholes with lengths indicated by the colour bar. The black line is a second order polynomial to the data gained for the polynomial interpolation $P2_v + P2_p$.

borehole radius (and correspondingly larger r_e) are solely controlled by mesh size and do not vary during a period (Fig. D3b). Consequently, the mesh size determined the apparent viscous skin depth leading to an overestimation of the damping coefficient.

D.3 Numerical results

D.3.1 Tight boreholes

The simulations for boreholes in a rigid and tight medium document a positive correlation between the radius of the borehole and the amount of time until the underdamped oscillation vanishes (Fig. D4a). Spectral analysis of the numerical results reveals that the pressure oscillates with the nominal eigenfrequency of a standing wave in a tube with one open end $f_0 = c_0/(4L)$ for small values of damping coefficients, that is $2\pi f_0 \gg \delta$. With increasing damping coefficient, for example due to a reduction in borehole radius, frequency decreases by up to 8 per cent compared to the nominal eigenfrequency (Fig. D4b and Table 3). The damping coefficients are overestimated—the more the larger R/ν —due to the described mesh problems (Fig. D4c).

D.3.2 Leaky boreholes

The numerical results for leaky boreholes are ‘consistent’ with those for tight boreholes in the sense that the frequency-damping relations for finite permeability converge to the ones for zero permeability. For leaky boreholes, amplitudes of the pressure oscillations decrease and damping coefficients increase with increasing permeability (Figs D5a and b). For the simulated full-length leaky boreholes ($L_{\text{leak}}/L = 1$), the frequency of the free pressure oscillations does not deviate much from that of tight borehole with the same length but slightly falls below the nominal eigenfrequency with increasing permeability (see Table 4 the first four rows). Damping coefficients from the numerical simulations are higher than the values predicted by eq. (2); the difference between both increases with the increase of R/ν values (indicative of mesh problems) and/or permeability (Fig. D6).

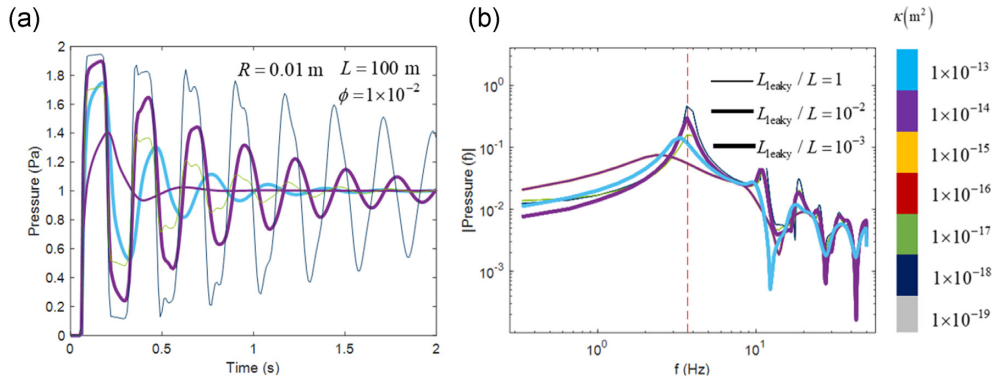


Figure D5. Pressure oscillations resulting from numerical simulations for leaky boreholes (length 100 m, radius 0.01 m, apparent porosity 1×10^{-2}) using the polynomial interpolating functions $P2_v + P2_p$: (a) time-series; (b) amplitude spectra. Permeability is indicated by the colour bars and the length of the leaky section by the indicated ratio L_{leaky}/L . The vertical red line in (b) represents the nominal eigenfrequency.

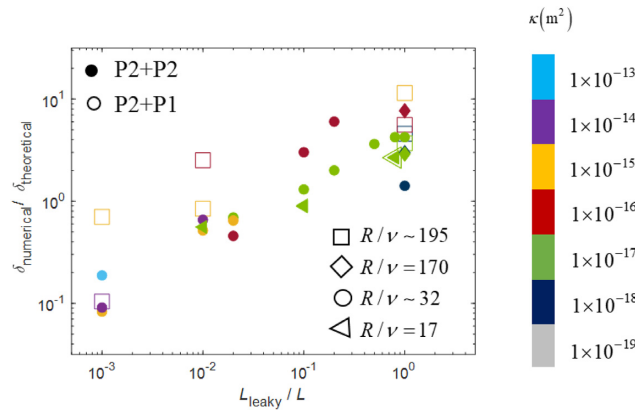


Figure D6. Ratio of damping coefficients from numerical simulations to theoretical predictions for leaky boreholes according to (2) as a function of the parameter L_{leaky}/L for different ratios of borehole radius and viscous skin depth (R/ν) reflecting differences in absolute length, and permeability values κ . The viscous skin depth is calculated using the fundamental frequency. Open and closed symbols represent simulations with polynomial interpolating functions $P2_v + P2_p$ and $P2_v + P1_p$, respectively, for velocity and pressure.

For partial-length leaky boreholes ($10^{-3} < L_{leaky}/L < 1$), the reduction in frequency from the nominal eigenfrequency depends on the length of the leaky section in addition to permeability as observed for full-length leaky boreholes (Fig. D5b). The damping coefficients increase with an increase in relative length of the interval, permeability, and the ratio R/ν (Fig. D6). However, the damping coefficients remain within the numerical limits corresponding to a tight ($L_{leaky}/L = 0$) and a full-length leaky borehole ($L_{leaky}/L = 1$) for a given R/ν value but not within the analytical limits because of the overestimation of damping due to the mesh problems (Fig. D7).

In leaky boreholes, overdamping, that is monotonous pressure decay, occurred for combinations of high permeability and long length of the leaky section and the occurrence is fairly consistent with the condition known for a harmonic oscillator $\delta \geq 2\pi f_0$ (Figs D5a and b). The permeability beyond which overdamping occurs depends on the contribution of wall friction. For a borehole with a radius of 0.18 m and a length of 1000 m, an underdamped oscillation occurred when the permeability was higher than $\kappa = 10^{-13} \text{ m}^2$. In contrast, for a borehole with the same length of 1000 m but a radius of only 0.01 m, the overdamping occurred for permeabilities above $\kappa = 10^{-17} \text{ m}^2$. The borehole with the small radius is already close to overdamping from the viscous dissipation alone; little additional damping due to leakage suffices to reach overdamping.

D.4 Implications for permeability determination

The numerical modelling confirmed that frequency and damping coefficient of free pressure oscillations contain information about the permeability of the medium penetrated by a borehole. For a full-length leaky borehole, the inversion of spectral components using (2) will result in a permeability $\kappa_{inverted}$ that coincides with the permeability κ of the porous medium. Inverted permeability should scale with the length of the leaky section of the borehole according to (3) when the borehole has partial leakage. Yet, the inverted permeability values surpass the values prescribed in the numerical model by up to 3 orders of magnitude as a consequence of the overestimation in damping coefficients; the larger the mesh size in comparison to the viscous skin depth the larger the overestimation (Fig. D8).

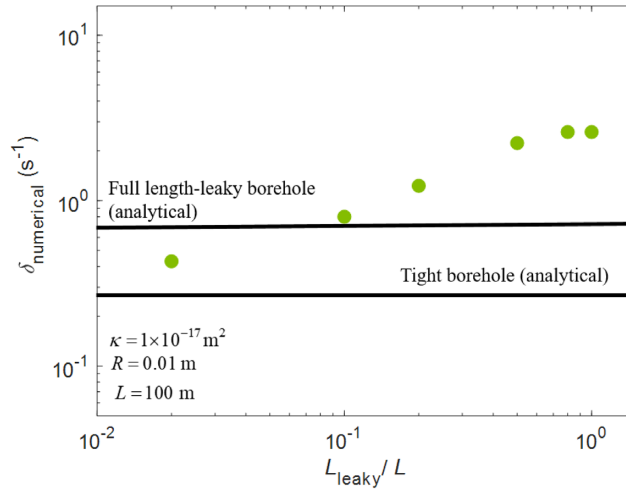


Figure D7. Damping coefficients of free pressure oscillation from numerical simulations as a function of relative length of the leaky interval. Length and radius of the borehole and permeability of the medium are indicated by the legend.

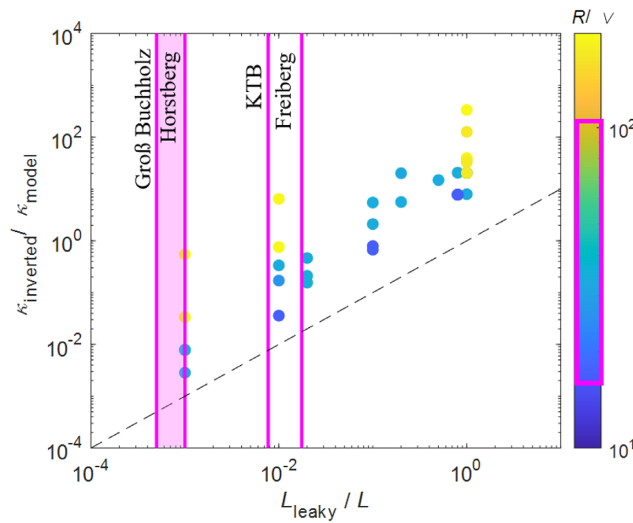


Figure D8. Ratio of effective permeability derived from spectral components of simulated free pressure oscillations, i.e. using (2), to actual permeability prescribed in the numerical model in COMSOL as a function of the relative length of the leaky section L_{leaky}/L . The colour bar indicates the ratio of borehole radius and viscous skin depth R/ν . The dashed black line represents the theoretical line according to (3). The vertical magenta lines and rectangle indicate the L_{leaky}/L and R/ν values of the field observations.

APPENDIX E

E.1 Axial and radial Strouhal numbers for fluid-flow waves in tight boreholes

In the dimensionless form of the Navier–Stokes equation, the terms related to inertial forces comprise the time derivative of the velocity field multiplied by the Strouhal number and the advective term. The Strouhal number expresses the ratio of the local acceleration of the flow to the advective acceleration and is given by

$$St = \frac{\tilde{l}f}{\tilde{v}}, \tag{28}$$

where \tilde{l} is the characteristic length and \tilde{v} is a characteristic velocity of the flow rather than the propagation velocity of the flow waves. The fluid motion associated with the pressure oscillation comprises an axial and a radial component and thus a Strouhal number for each velocity component. We used the maximum value of the fluid velocity components to calculate a lower bound of the Strouhal numbers. Using the maximum axial velocity $U(r = 0) = P_0 k_z / \rho_f \omega$ we obtain:

$$St_{axial} = \frac{c_0^2 \rho_f}{n P_0}, \tag{29}$$

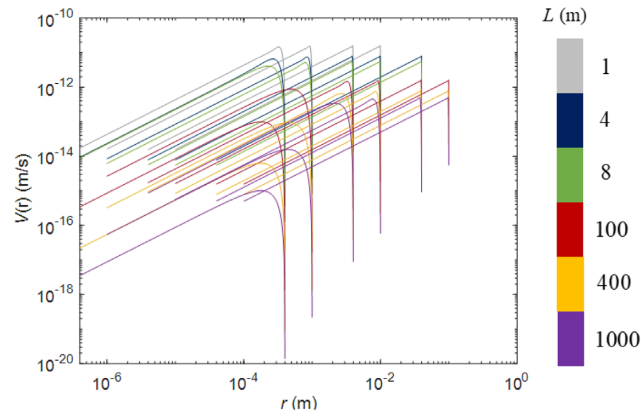


Figure E1. Real part of the radial velocity in a tight borehole calculated for different fundamental frequencies ($f_0 = c_0/4L$) as a function of radial position for different borehole radii and lengths (colour bar) used in the numerical simulations. The sharp velocity decays close to the borehole radius reflects the imposed no-slip boundary condition.

with $n = 2$ or $n = 4$ for a closed or an open end, respectively. The maximum value of the radial velocity is more difficult to obtain analytically, so we took the maximum value of the real part of the radial velocity (15) evaluated for the radius and frequencies used in the numerical simulations (Fig. E1).

APPENDIX F

F.1 Effect of end condition on the frequency of flow waves in tight boreholes

A flow wave traveling in a filled borehole with finite length will be reflected at each end. The superposition of the waves travelling in opposite direction gives rise to standing waves. The condition of the two ends, here addressed as upstream and downstream for distinction, represents a boundary condition for the flow rate. The amplitudes of the upstream (U) and downstream (D) flow rates are not the same due to storage effects in the borehole and are given by eqs (53) and (54) in Bernabé (2009) as

$$Q_U = -i \frac{\pi R^2}{\rho c} \frac{P_U \cos\left(\frac{\omega L}{c}\right) - P_D}{\sin\left(\frac{\omega L}{c}\right)} \left(\frac{2J_1(\kappa R)}{\kappa J_0(\kappa R)} - 1 \right) \quad (30)$$

and

$$Q_D = -i \frac{\pi R^2}{\rho c} \frac{P_U - P_D \cos\left(\frac{\omega L}{c}\right)}{\sin\left(\frac{\omega L}{c}\right)} \left(\frac{2J_1(\kappa R)}{\kappa J_0(\kappa R)} - 1 \right). \quad (31)$$

In our field tests, the closure of the valve at the wellhead or the injection line excites the oscillation and corresponds to a closed-end condition with

$$Q(t, z = 0) = Q_U e^{i\omega t} = 0. \quad (32)$$

The opposite end might correspond to anything between open or closed condition depending on the specific problem, for example the double-packer interval at the end of a coiled tubing is not a closed end but neither truly open. As common in hydraulic laboratory experiments, we address this opposite end as the downstream and characterize it by its storage capacity S_D , with $S_D \rightarrow \infty$ for an open end and $S_D \rightarrow 0$ for a closed end. The boundary condition for the downstream, see appendix A in Bernabé (2009), is then given by

$$Q(t, z = L) = Q_D e^{i\omega t} = -i\omega S_D P_D e^{i\omega t}. \quad (33)$$

Substituting (32) into (30) and (33) into (31), two expressions for the pressure–amplitude ratio are obtained:

$$Q_U = -i \frac{\pi R^2}{\rho c} \frac{P_U \cos\left(\frac{\omega L}{c}\right) - P_D}{\sin\left(\frac{\omega L}{c}\right)} \left(\frac{2J_1(\kappa R)}{\kappa J_0(\kappa R)} - 1 \right) = 0 \\ \Rightarrow \frac{P_D}{P_U} = \cos\left(\frac{\omega L}{c}\right) \quad (34)$$

and

$$Q_D = -i \frac{\pi R^2}{\rho c} \frac{1 - \frac{P_D}{P_U} \cos\left(\frac{\omega L}{c}\right)}{\sin\left(\frac{\omega L}{c}\right)} \left(\frac{2J_1(\kappa R)}{\kappa J_0(\kappa R)} - 1 \right) = -i\omega S_D \frac{P_D}{P_U}. \quad (35)$$

Combining (34) and (35) and using the expression (1), we find

$$\frac{\omega L}{c} \left[\tan\left(\frac{\omega L}{c}\right) + \frac{S_D \rho c_0^2}{\pi R^2} \frac{\omega}{c} \right] = 0, \quad (36)$$

Relation (36) is satisfied only for real arguments in the tangent function; the possible fluid wave velocities depend on the storage capacity of the downstream reservoir. Specifically, for the cases of open and closed borehole, (36) gives

$$\tan\left(\frac{\omega L}{c}\right) = - \begin{cases} 0 & \text{for } S_D = 0 \text{ for closed end} \\ \infty & \text{for } S_D = \infty \text{ for open end} \end{cases} \quad (37)$$

Eq. (36) is satisfied when

$$\tan\left(\frac{\omega L}{c}\right) = \begin{cases} 0 \Rightarrow \frac{\omega L}{c} = m\pi \Leftrightarrow \hat{f}_m = \frac{mc}{2L} = m\hat{f}_0 \\ \infty \Rightarrow \frac{\omega L}{c} = \frac{2m+1}{2}\pi \Leftrightarrow f_m = \frac{(2m+1)c}{4L} = (2m+1)f_0 \end{cases}, m = 1, 2, 3, \dots \quad (38)$$

corresponding to the classical organ-pipe relations:

$$*P2_v + P1_p.$$